Rapid acquisition of internal models of timing by Purkinje cells enables faster behavioral responses

Sriram Narayanan[1], Aalok Varma[1], and Vatsala Thirumalai[1#]

[1]National Centre for Biological Sciences, Tata Institute of Fundamental Research, Bangalore 560065, India.

Keywords: internal models, Purkinje neurons, prediction error, zebrafish, optomotor, calcium imaging

Number of words: Summary: 147, Introduction: 1032, Results: 4341, Discussion: 1332, Methods: 3743.
Number of Figures: 8
Number of Supplemental Figures: 7
Tables: 2
Videos: 2

#Corresponding author: vatsala@ncbs.res.in

Acknowledgements: The authors would like to thank the following sources of funding support: Wellcome Trust-DBT India Alliance Intermediate and Senior fellowships (VT), Department of Biotechnology (VT), Science and Engineering Research Board, Department of Science and Technology (VT), Department of Atomic Energy (VT), NCBS-TIFR graduate student fellowship (SN and AV). The authors would also like to thank Prof. Masahiko Hibi for providing the Tg(aldoca:GCaMP6s);nacre-/- fish line. Further thanks are also due to Mr. T.P. Jagadeesh for the maintenance of our fish lines and to Drs. Lena Robra, Mehrab Modi and Ebi George for providing advice and assistance. In addition we would like to thank the Central Imaging and Flow Facility at NCBS for support.

Highlights

- Larval zebrafish learn the timing of optic flow stimuli with minimal sensory evidence.
- The cerebellum performs an innate, hitherto unknown, supra-second timing function.
- Purkinje cells use prediction errors to acquire an internal model of stimulus timing.
- Robust predictions lead to faster reaction times when stimulus arrives as expected.

Summary

Neural mechanisms that allow animals to keep track of multi-second time intervals are not clearly understood. Further, the role of the cerebellum in this process is under debate. We show that when periodic optic flow is presented, cerebellar Purkinje cells in larval zebrafish show simple spike and climbing fiber activity that ramps up in anticipation of flow onset. A distinct subset of Purkinje cells reports prediction error signals mediated solely by climbing fiber inputs when the stimulus interval is altered. These signals develop in 2 trials and can quickly adapt to new intervals if stimulus timing is altered. Robust predictive and prediction error signals are associated with faster behavioral responses and the modulation of behavioral latency is dependent on the cerebellum. Based on our results, we built an algorithmic model that explains how Purkinje cells mediate acquisition and updating of an internal model of stimulus time intervals.

Introduction

Animals can discriminate time intervals ranging from microseconds to days, which serves to regulate functions as diverse as sound localization to circadian rhythmicity, respectively (Mauk and Buonomano, 2004; Buhusi and Meck, 2005; Buonomano, 2007). While the mechanisms that enable temporal processing at the microsecond and day scales are relatively well understood (Jeffress, 1948; Rosbash and Hall, 1989), those that enable animals to discriminate time in the intermediate time scales are not at all clear. Temporal discrimination in the hundreds of milliseconds to minutes range, referred to as interval timing, is behaviorally salient as most foraging behaviors, decision-making tasks and mating rituals occur over these time scales. The ability to track the passage of time in this range is critical for anticipating events, for learning associations between stimuli and for planning motor actions (Buhusi and Meck, 2005; Buonomano, 2007; Merchant and de Lafuente, 2014; Paton and Buonomano, 2018).

Neuropsychological and neuroimaging studies in healthy subjects and patients with neurological conditions led to the idea that there might be at least two distinct interval timing mechanisms, one involving the cerebellum for the "automatic" sub-second range (Ivry and Keele, 1989; Spencer and Ivry, 2013) and another, which is independent of the cerebellum but dependent on cortico-basal ganglia circuits for the "cognitively-controlled" supra-second range (Lewis and Miall, 2003a, 2003b; Malapani et al., 1998a). Nevertheless, cerebellar damage in humans has been shown to affect reproduction of time intervals in the multiple seconds scale (Malapani et al., 1998b). Experiments in animal models have shown clearly a requirement for cerebellar circuits in sub-second timing such as those seen during classical eye-blink conditioning (Koekkoek et al., 2003; McCormick and Thompson, 1984; Medina et al., 2000) but whether the cerebellum might play a more general role in timing function at longer intervals is not yet clear (Kunimatsu et al., 2018; Ohmae et al., 2017). Given the primacy of cerebellar function in sensori-motor processing, we sought to understand if a central role for the cerebellum in sensori-motor timing at behaviorally relevant supra-second time intervals might have been overlooked.

Additionally, several models have been proposed to explain how neural circuits might encode time, including oscillator-based (Gibbon, 1977; Miall, 1989), state-dependent networks (Karmarkar and Buonomano, 2007), population clocks (Medina et al., 2000), and ramping firing

rates (Simen et al., 2011). Intrinsic and synaptic dynamics of neurons enable them to function as efficient 'clocks' using any of the above mechanisms. It is possible that different brain regions encode time using distinct mechanisms. With this in mind, we explored how cerebellar neurons represent behaviorally salient time intervals.

The cerebellum is one of the oldest parts of the vertebrate brain, with cell types and connectivity well conserved in all vertebrates from fish to mammals (Bae et al., 2009; Bell et al., 2008). In larval zebrafish, the cerebellum is functional by 5 days post-fertilization concomitant with the emergence of motor behaviors (Sengupta and Thirumalai, 2015). At these stages, the larva is transparent, allowing the imaging of dorsally placed Purkinje cells, which are the principal neurons of the cerebellar cortex. Since there are fewer Purkinje cells in larval zebrafish compared to mammals (Hamling et al., 2015; Knogler et al., 2019), using in vivo imaging, it is possible to capture the activity of a significant proportion of Purkinje cells during motor behaviors involving interval timing.

Among the motor behaviors generated by larval zebrafish, is the optomotor response (OMR), an innate reflex response believed to help stabilize their position in flowing water (Neuhauss et al., 1999; Orger et al., 2000). Larvae use optic flow to sense if water currents are destabilizing them and generate compensatory swims to stabilize themselves until the visual drift is minimized. OMR can be evoked in head-restrained larvae (Portugues and Engert, 2011; Jha and Thirumalai, 2020) and they remain responsive if the optic flow stimulus is coupled in closed-loop to the motor output (Ahrens et al., 2012; Mu et al., 2019; Portugues and Engert, 2011). We probed whether larval zebrafish can learn supra-second time intervals when repeating flow on-off OMR stimuli are presented to them in a fixed pattern. If the time intervals are indeed learnt, larvae will be able to predict the next stimulus and also register an error if the pattern deviated from the expectation.

Neural activity corresponding to predictions and prediction errors has been recorded from Purkinje cells during different association tasks. Purkinje cells receive excitatory inputs primarily from two sources, climbing fibers (CFs) from the inferior olive and parallel fibers (PFs) from granule cells. Single CF inputs cause large, easily detectable changes in GCaMP fluorescence in

Purkinje cells whereas PF mediated changes in simple spike (SS) rates contribute to a much smaller fraction of the GCaMP signal (Kitamura and Häusser, 2011; Knogler et al., 2019; Sengupta, 2015). Both CF and PF inputs have been shown to convey distinct information to Purkinje cells in a number of behavioral paradigms: In tasks where associations between a cue and a reward is learnt, CFs have been shown to be predictive of reward (Heffley and Hull, 2019; Kostadinov et al., 2019). CFs also convey a prediction error signal when a reward is expected, but does not occur (Kostadinov et al., 2019). PFs convey to Purkinje cells a rich representation of the sensorimotor environment and also signals predictive of motor timing or timing of reward (Giovannucci et al., 2017; Knogler et al., 2017; Wagner et al., 2017). However, studies so far have focused on predictive functions of the cerebellum primarily in the sub-second range.

In this study, larval zebrafish learnt time intervals spanning several seconds in the context of an innate reflex response and used such predictions to drive motor behaviors. Intervals were learnt in behaviorally relevant timescales without the need for extensive training. Using GCaMP imaging and electrophysiology, we teased apart contributions of CF and SS to predictions and prediction errors. Our results demonstrate that distinct functional subcircuits in the cerebellum are involved in acquiring and updating internal representations of optic flow timing and in using them for motor planning. Further, we observe entrained oscillatory and ramping activity in these two sub circuits corresponding to learned stimulus timing and motor timing. We present an algorithmic model of the timing mechanism to explain the results of our experiments.

Results

An interval timing task for larval zebrafish

We placed 7-8 day old zebrafish larvae in a closed-loop optomotor track (Figure 1A) and presented regularly timed optic flow stimuli to them (Figure 1B). One trial consisted of an optic flow-on period of 2s followed by a 5s inter-trial interval (ITI) with no optic flow (Figure 1B). During the optic flow-on period, the gain of the closed loop feedback was set to provide realistic visual feedback during swim bouts to maintain consistent levels of behavioral responsiveness (Mu et al., 2019; Portugues and Engert, 2011). Fish were presented with 100 trials out of which 10% of trials chosen pseudorandomly were probe trials, in which optic flow was not presented, resulting in a deviation from the predominantly experienced pattern (Figure 1B). Probe trials

were used to look for behavioral and neural signatures of fish learning the time intervals between successive flow-on stimuli. The behavior setup was incorporated into a custom two-photon microscope to simultaneously image calcium activity in Purkinje cells during the behavior assay (Figure 1A, C, D). Activity profiles of Purkinje neurons with respect to optic flow or probe trials were analyzed offline (Figure 1E).

Fish swam preferentially in the 2s optic flow-on periods with a median latency of around 1.2 s after the optic flow was turned on (Figure 1F, H) and seldom during the 5s ITI when stationary gratings were presented, indicating that swim bouts were initiated in response to optic flow. No swimming was observed in probe trials in the absence of optic flow (Figure 1F, G). We surmised that in the absence of optic flow input or motor output during probe trials, neural activity occurring in this window might reveal processes involved in interval timing.

Purkinje neurons encode a widespread, time-locked prediction error signal

To look for indications in neural activity that optic flow timing is predicted, we simultaneously imaged calcium activity in Purkinje neurons expressing GCaMP6s (Chen et al., 2013), using a custom two-photon microscope. Calcium activity in a single optical plane with 69 ± 14 (mean ± SD, Figure S1) cells was recorded through each experiment, accounting for 15-20% of the total number of Purkinje cells at this stage of development (Hamling et al., 2015; Knogler et al., 2019). Upon visual inspection, a significant fraction of cells showed a response to optic flow (Figure 2A, left), caused by sensory input, motor activity or both. There was also a surprisingly widespread signal, time-locked to the expected optic flow-on time in probe trials (Figure 2A, right; Video S1). We then classified cells into 9 clusters based on their average optic flow and probe responses using correlation based hierarchical clustering (Antinucci et al., 2019). 5 distinct clusters, namely clusters 2, 3, 4, 5 and 8, were found based on the intersection between the independently generated optic-flow and probe response types (See Methods). 1573 out of all of the 1874 cells we recorded from could be classified into one of the 5 clusters. 954 out of 1573 cells belonged to cluster 4, with strong responses to optic flow and no response during probe trials (Figure 2B-D). Clusters 2, 3, 5 and 8 showed large responses during probe trials (Figure 2B). The probe responsive clusters also showed significant changes in activity during non-probe trials but their optic flow responses were significantly lower in amplitude than the probe

responses (Figure 2C). The mean response amplitude of cluster 3 cells during probe trials was similar to non-probe trials due to the lower response probability during probe trials (Figure 2C, D). Probe triggered responses in all probe responsive clusters were time-locked to the expected onset time of optic flow (Figure 2E, Table S1). To further confirm that the probe responses were indeed specific to the expected onset time of optic flow, we looked at all 1874 cells we recorded from for any increase in activity in a window -2s to 4s from the onset of probe trials. An increase in activity was defined as any period of 1s within the window where the mean dF/F crossed 3 SDs above a 1s long pre-window baseline. A cell was chosen if it crossed the threshold in at least 3 probe trials. The responses we found using this method were also those tuned to the expected onset time of optic flow (Figure S2; 620 cells, 23 ± 8 cells per fish (mean ± SD)), confirming the temporal specificity of the probe response. These results clearly show that Purkinje cells encode a widespread and time-locked prediction error (PE) signal.

PE signals are acquired rapidly

The existence of these PE responses in Purkinje cells is evidence that larval zebrafish can learn time intervals between behaviorally relevant sensory inputs. To estimate the time course over which larvae learn to predict such time intervals, we looked at individual probe trials and calculated the probability of a cell exhibiting a PE signal and the amplitude of the signal when it occurred, without trial averaging (See Methods). Contrary to our expectation, neither probability nor amplitude of the PE signal showed an increase over the course of the experiment (Figure 2F, G). The very first probe trial, presented after two consecutive trials of optic flow, had a PE signal indistinguishable from probe trials later in the experiment (Figure 2F, G; Figure S3). The onset of the PE signal was rapid and did not change in probability or amplitude over the course of the experiment. Clusters 2, 3, 5 and 8 were pooled together for this analysis since we did not find differences between them. In summary, a significant fraction of Purkinje cells encode a time-locked PE signal, which is acquired quickly with minimal sensory evidence, in 2 trials.

Purkinje cells encoding PE signals perform a motor-independent timing function

Next we asked whether the timing function performed by Purkinje cells encoding PE signals depends on motor activity. Fish showed varying levels of behavioral arousal in the closed loop optomotor arena, quantified by the total number of swim bouts and minimum latency to respond

to optic flow (Figure 1F). Minimum latency was calculated as the minimum value of the 10 trial moving average of latencies across all trials for each fish. Both these behavioral variables were highly anticorrelated, with fish that generated more swim bouts also showing lower minimum latencies (Figure 3A). Thus fish eliciting swim bouts regularly during the optic flow-on period with low latencies can be considered to more aroused than those that are not. Similarly we used trial-wise PE response probability and the number of probe-responsive cells as indicators of the strength of the PE signal. We hypothesized that if PE signals are indeed related to the state of motor arousal, then the behavioral variables will be correlated with the strength of the PE signal. We found that this was not the case: the probe-responsive cluster (clusters 2,3,5 and 8) failed to show any correlation of the mean PE response probability with either number of bouts or minimum latency (Figure 3B, D). Similarly, there was no correlation between the number of probe responsive cells in the cluster and either number of bouts or minimum latency (Figure 3C, E). These results hold true when the correlations were calculated for individual clusters as well (Figures S4 and S5). This indicates that Purkinje cells involved in encoding PE signals are performing a non-motor function and are involved in acquiring and updating predictive models of optic flow timing irrespective of whether motor output will be generated using them.

Optic flow timing is represented in entrained neural activity and is adaptable

If PE signals result from the larva having learnt the interval between optic flow timing, we would expect to see PE signals that are well timed over multiple probe trials before they are extinguished (Sumbre et al., 2008). To test this, we presented a set of fish with 20 trials of optic flow of 2s duration with a 5s ITI, followed by 10 consecutive probe trials (Figure 4A). Each experiment consisted of 5 repeats of this stimulus pattern, with no gaps in between them. As observed earlier, almost no swim bouts were observed during the 10 consecutive probe trials (Figure 4A). We then filtered cells with three broad response properties using regressors made by convolving the stimulus waveform with a GCaMP6s kernel (Miri et al., 2011). Three regressors were made, the first one representing the optic flow stimulus, the second representing a response to optic flow that remains entrained during the extended probe phase and the third representing an entrained PE signal that is suppressed during the optic flow-on phase (Supplementary Figure 6A-top). These response profiles broadly represent the clusters observed in Figure 2. Cells were classified based on cross correlation with the three regressors as optic

flow driven, entrained or PE with a threshold correlation coefficient of 0.3 required for classification (Figure S6A-bottom). A significant fraction of cells could be classified into the three groups in each fish, with 31 ± 6 (mean ± SD) cells showing a strong optic flow response and no PE signal, 3 ± 1 cells showing an entrained response and 6 ± 2 cells showing an entrained PE signal (Figure 4A, Figure S6A-C and Video S2). Cells showing strong optic flow response were similar to cells in cluster 4 (Figure 2B) and showed no significant correlation with the PE regressor (Figure S6A, F). Since by definition, cells with high correlation coefficients with optic flow or PE regressors are likely to have high correlation with the entrained response regressor, we classified cells as entrained only if they had suprathreshold entrained correlation and subthreshold optic flow and PE correlations (Figure S6A-bottom, D-F). Out of the cells that showed entrained responses, the responses were either more 'optic flow like' or 'PE like' (Figure S6G-I).

Cells showing significant correlation with the PE regressor had responses that remained time-locked to the expected onset times of optic flow in each of the 10 probe trials (Figure 4A, B and Table S2). The PE signal exhibited a detectable initial decay, but subsequently remained robust across the 10 probe trials, with comparable response probabilities and amplitudes throughout the extended probe period (Figure 4A, C, D). Statistically, the PE response probability showed a significant decay from the first probe trial compared to baseline (Figure 4C, $p = 0.008$, Wilcoxon signed-rank test, 10 fish) and was weakly elevated again in trial 7 ($p = 0.025$). No other trials showed significantly different response probability compared to baseline. Similarly, the PE response amplitude showed weak but significantly elevated values over baseline in probe trial 2 (Figure 4D, $p = 0.027$, Wilcoxon signed-rank test, 10 fish). No trend was observed over the 5 repeats in mean response probability or amplitude (Figure 4E, F). Baseline was estimated as the 25th percentile of the averaged data points.

The presence of entrained PE signals over multiple probe trials indicates that the larva has learned the interval between successive optic flow on periods. For such a predictive mechanism to be ethologically relevant, it should be able to adapt quickly to changes in the stimulus timing. We tested this by varying the ITI after 60 trials from 5s to 7s, without any additional gap between the two blocks of 60 trials each. We selected cells that showed at least one PE signal for

the 5s ITI and looked at probe triggered averages for these cells during the 7s ITI. The PE signal switched to the 7s ITI within the first probe trial (Figure 4G, H), which was either the third or ninth trial after the switch. Thereafter, the PE signal remained stable for the 7s ITI (Figure 4G, H).

Results from the above experiments provide strong evidence for an entrainment based mechanism in predicting optic flow timing. The entrainment continued for at least 70s without sensory cues, with a detectable but small decay in strength, but is capable of rapidly adapting within 4 trials to new intervals to match changes in the environment.

Electrophysiological correlates of prediction and error signals in Purkinje cells

To identify the input sources to Purkinje cells contributing to PE signals and possibly predictive signals used to plan motor commands, we performed loose-patch recordings from paralyzed fish that were engaged in the same behavior assay as above (Figure 5A, left). Single CF inputs cause large, easily detectable changes in GCaMP fluorescence in Purkinje cells whereas PF mediated changes in simple spike (SS) rates contribute to a much smaller fraction of the GCaMP signal (Kitamura and Häusser, 2011; Knogler et al., 2019; Sengupta, 2015).

Extracellular recordings from Purkinje cells revealed small amplitude simple spikes (SS) and larger amplitude CF inputs (Sengupta and Thirumalai, 2015) (Figure 5A, right). We sorted SS and CF events and analysed how they are modulated during probe trials and flow trials (See Methods). A significant elevation in CF rates compared to baseline was observed in probe trials in 5 out of 20 cells (Figure 5B, C), with these cells also showing high modulation indices: 0.51 ± 0.31 (Mean ± SD). These 5 cells when taken together showed a significant increase in CF rate during probe trials compared to baseline (Figure 5C). 4 cells showed significant elevation in SS rates compared to baseline (Figure 5B, D), but with very low modulation indices: 0.14 ± 0.14 (Mean ± SD). The SS rate for these 4 cells when grouped together was not significantly different during probe trials compared to baseline (Figure 5D) and the low SS probe trial modulation indices are unlikely to cause the large amplitude PE signals observed in calcium imaging. These results strongly indicate that PE signals are encoded in CF inputs to Purkinje cells which result in the large calcium responses seen in probe trials. Moreover, despite the large differences in

sample size, the proportion of cells exhibiting strong PE responses was comparable when assayed with calcium imaging or electrophysiology (33% with calcium imaging and 25% with electrophysiology).

The presence of robust PE responses in Purkinje cells is possible only if there are neural signals predicting the timing of the next optic flow onset. As shown in Figure 4A, a few Purkinje cells are entrained to optic flow onset. With the higher temporal resolution of extracellular recordings, we wished to determine if there are more prevalent signatures of predictions of optic flow timing among Purkinje cells.

All cells showed positive SS modulation indices during optic flow compared to baseline (Figure 5E, F). CF inputs were positively modulated by optic flow in 15 out of 20 cells (Figure 5E, G) and strongly negatively modulated in the remaining 5 cells (Figure 5E, J). We separated cells based on the sign of their modulation index for further analysis. Both CF and SS rates in cells with positive modulation indices showed a significant pre-trial ramp (Figure 5H, I) leading up to the onset of the trial and could possibly represent an entrained predictive signal. Cells with negative CF optic flow modulation indices showed high pre-trial CF rates that were suppressed almost completely by optic flow (Figure 5J). The suppression was absent in probe trials (Figure 5J) and occurred significantly before the onset of motor activity (Figure 5K), indicating a possible role for these cells in predicting optic flow timing, rather than motor control. Similar anticorrelated activity can be seen in cluster 2 cells in the calcium imaging experiments.

These results strongly indicate that PE signals are encoded in CF inputs from the inferior olive. The pre-trial ramping in both SS and CF rates seen here (Figure 5F-I) possibly represents predictive activity entrained to the learned time intervals.

Prediction and error signals in Purkinje cells regulate swim bout latency

Thus far, we have shown that Purkinje cell activity encodes predictive and prediction error signals when optic flow stimuli repeating at defined time intervals are presented. To analyse how the cerebellum uses this predictive information to modulate behavioral responses to optic flow, we measured the latency to initiate swim bouts in the closed loop paradigm using the 5s ITI

(Figure 6A). This analysis was performed on behavior data collected from the experiments whose results from neural recordings are shown above in Figures 2 and 3. In fish with an intact cerebellum, latency to generate a swim bout was significantly higher in the trial immediately following the probe trial (Figure 6B) with respect to a pre-probe baseline. This implies that fish use the learned inter-trial interval information to predict flow onset and this leads to faster behavioral output. Occurrence of a probe trial might might weaken or update previously learnt predictions of optic flow timing and delay swim bout initiation. We then lesioned the cerebellum and repeated the above experiment (Figure 6C). Probe trials did not cause a transient elevation in latency in cerebellum-lesioned fish (Figure 6D). Both lesioned and non-lesioned fish showed similar levels of behavioral responsiveness (Figure 6E,F). The cerebellum-dependent elevation in latency caused by probe trials indicates a specific role for the cerebellum in modulating behavioral responses on a trial-by-trial basis, using predictions of optic flow timing. To probe this further, we independently looked at how both PE signals and pre-trial activity correlate with swim bout latency on a trial by trial basis.

First, we hypothesized that the robustness of the PE signal during a probe trial reflects robustness with which the ITI is being predicted. In turn, robust ITI prediction is expected to lead to shorter swim bout latency after flow onset (Figure 6B). Figure 7A shows the same Purkinje cells from one fish imaged in two trials, with the trial shown on top having a PE response probability of 0.26 and an average swim bout latency around this probe trial of 0.74 s while the one shown in the bottom has a PE response probability of only 0.04 and a much longer average latency of 1.57 s. To establish the relationship between PE response probability and swim bout latency across all fish, we measured the correlation coefficient between these two parameters using the following method. Since probe trials constituted only 10% of all trials, we linearly interpolated the PE probability between probe trials to obtain an indirect, coarse-grained estimate of the robustness of internal representations of ITI throughout the experiment (Figure 7B, red trace). Similarly, latencies were also linearly interpolated and smoothened with a rolling average of 10 trials before computing the correlation coefficient. The 10 trial smoothing window matches the average distance between probe trials, thereby yielding a comparably coarse-grained estimate of latency (Figure 7B, black trace). Fish that paused swimming for >10 consecutive trials at any point during the experiment were excluded to minimize interpolation artifacts. We then

computed the correlation coefficient between the interpolated PE response probability and smoothed swim bout latency. 12 out of 16 fish showed significant negative correlations between interpolated PE probability and latency compared to chance. Of the remaining 4 fish, 2 showed significant positive correlations and 2 fish did not show significant correlations. Overall, the population showed a significant negative correlation between interpolated PE probability and latency (Figure 7B,C). These results show that robust PE signals observed during probe trials, indicative of a strong internal model of the ITI, are associated with lower latency to respond during optic flow trials. This also strongly suggests that predictive information might be used to plan motor commands to be executed when optic flow is encountered as expected.

Observations from loose-patch recordings show an entrained pre-trial ramping in SS and CF rates (Figure 5H, I) that could potentially encode either the timing of arrival of the next optic flow stimulus or preparedness to swim in response to optic flow if it arrives as expected. In either case, this pre-trial ramp up in activity will also be stronger for robust internal models of the ITI and therefore correlate with shorter latencies, similar to the relationship with PE response probability. To test whether this is true, we looked at whether the average population activity in the calcium imaging frame prior to the onset of optic flow predicted latency from trial onset. The pre-flow population activity averaged across all cells in individual fish showed a significant negative correlation with latency from trial onset (Figure 7D, grey traces are for individual fish). There was no correlation when trial order was shuffled (Figure 7E). To get a better understanding of what functional cell types were involved, we grouped cells into the functional clusters identified earlier (Figure 2B) and looked at clusterwise correlations between pre-flow population activity and latency. The pre-flow population activity in cluster 4 was responsible for the correlation observed when all cells were pooled together (Figure 7F,G). Cells in cluster 4 show large calcium responses to optic flow and do not show PE signals (Figure 2B,D). Significant predictive information about latency was present in pre-flow population activity in cluster 4 upto 2.5s prior to the onset of a trial (Figure 7H), indicating that these cells encode activity that is involved in motor planning well before the onset of optic flow. This is consistent with the observation from loose-patch recordings where an entrained increase in SS and CF rates was observed seconds before trial onset (Figure 5H,I). There was no correlation when we independently tested the other clusters (Figure S7).

These results reveal two distinct functional subcircuits in the cerebellum, one that encodes predictive activity entrained to stimulus timing in the environment (cluster 4) and another that manifests an error signal when the expected stimulus does not occur (clusters 2, 3, 5 and 8). On a trial-to-trial basis, the entrained predictive activity feeds into motor planning resulting in faster behavioral responses while the error signals are used to update internal models that are no longer valid.

Algorithmic model explains the acquisition of predictive timing representations and their behavioral consequence

We built an algorithmic computational model to explain how adaptable timing representations are acquired and used to drive behavior (Figure 8A). The model is based on a conceptual framework supported by the experimental data reported above. Specifically, we used the following observations to constrain the model: (1) the learnt time interval (internal model) is encoded in entrained neural activity (Figure 4A); (2) a robust prediction error (PE) response is generated when predictions of the internal model do not match inputs from the real world (Figure 2B); (3) the internal model is acquired and adapted with minimal sensory evidence (Figs. 2B, S3, and 4G); and (4) PE responses inhibit locomotor drive, leading to longer latency after probe trials (Figure 6B). In addition, there may be other processes which are not explicitly included in our model: (1) In the continued absence of novel ITIs, previously learnt ITIs are maintained (Figure 4). This could be conceptualized by a state variable that gates updating of the internal model ('State' and grey lines in Figure 8A). (2) Activity that precedes flow onset feeds into mechanisms of motor planning (Figure 6D-H). Since this is not directly involved in the encoding of time intervals, we did not include this process in our model.

The model was set up as described below and in the methods section (Figure 8A) and simulations were carried out with 0.01s time steps. There were two inputs to the model, optic flow stimuli F_{in} and a preset periodic response E, with a dynamic inter-burst interval (IBI) and 2s long bursts, representing the entrained internal model of the ITI. PE was calculated from the temporal difference between E and F_{in} (see Methods). When the predicted interval is too short, PE is positive and when the predicted interval is too long, PE is negative. Flow responses and

probe responses, recapitulating experimentally observed cell classes (Figure 2B) could be simulated by convolving F_{in} and PE signals with the GCaMP6s kernel (Figure 8B, C, E). In each time step, the IBI of E was updated by a learning rule (see Methods) using PE feedback. Briefly, the direction and duration of PE responses lead to adjustment of the internal model until a close match is achieved (Figure 8D). When PE is positive, the predicted time interval (IBI) is increased, and when PE is negative, IBI is shortened. We first tested the model with the stimulus interval fixed at 5s and the internal model IBI was initiated with a range of values from 2s to 29s. Irrespective of the starting IBI, the model always converged to the stimulus interval in timescales comparable to those observed experimentally. Conversely, we fixed the internal model IBI at 5s and varied the stimulus interval between 2 and 29s, recapitulating the experiment shown in Figure 3G. Here too, the model converged to the stimulus interval quickly (Figure 8D) and exhibited well timed PE signals within 4 trials (Figure 8E, first probe), as observed experimentally.

PE signals are useful not only to track the stimulus intervals but also to adjust behavioral responsiveness. Swim latencies are transiently elevated following the occurrence of PE signals (Figure 6B). This suggests that PE signals inhibit locomotor drive, either directly or by updating the internal model used to predict optic flow onset in the next trial, thus delaying the next swim bout. We modeled the locomotor drive variable M as a leaky integrator of optic flow stimulus and the absolute value of PE (Figure 8A). Swims are generated when M crosses a pre-fixed threshold value, picked to reflect naturally occurring swim latencies (see Methods). M increases when optic flow is present and is inhibited by non-zero PE (Figure 8A). Latency modeled this way showed a transient elevation after probe trials (Figure 8F) similar to the experiments (Figure 6B).

To summarize, using simple, neurally-implementable algorithms, we were able to recapitulate most features of neural activity and behavior we see in our experiments. This model shows how entrained predictive responses can be used to generate error signals we see in the cerebellum and implements a robust learning rule to adaptively learn a range of stimulus timings with minimal sensory evidence. The model also shows how PE signals can feed into the motor system to adjust behavioral responsiveness by inhibiting locomotor drive. In sum, our experimental and modeling

results indicate the existence of robust neural mechanisms in larval zebrafish for learning behaviorally relevant time intervals in the seconds range.

Discussion

Using calcium imaging and loose patch recordings of Purkinje cells during repeating optic flow stimuli, we showed that the cerebellum is actively involved in the acquisition and updating of internal representations of behaviorally-relevant supra second time intervals. We found two distinct sub-classes of Purkinje cells, one class (cluster 4) shows ramping activity prior to the onset of optic flow stimulus, and a large increase in SS and CF activity in response to optic flow; and another (clusters 2,3,5,8), which has modest optic flow responses but large increase in CF activity when optic flow is expected, but does not occur at the expected time (PE signals; Figures 2 and 5). We propose that these two classes of Purkinje cells participate in predictive control of behavior and acquisition of internal models of interval timing respectively. High confidence in the learned time interval is reflected by strong predictive activity in cluster 4 Purkinje cells and wider representation of prediction error responses in clusters 2,3,5 and 8. Higher confidence in turn correlates with lower latency to respond (Figure 7) reflecting a readiness of the motor system to act when optic flow stimulus is encountered as expected. However, when there are unexpected deviations in the stimulus pattern, such as during probe trials, confidence in the learned time interval is reduced, and latency is transiently elevated in the subsequent trial (Figure 6B). Lesioning the cerebellum eliminates this transient elevation in latency (Figure 6D). Based on these results, we propose that the cerebellum is involved in learning and readjusting internal models of stimulus timing.

Strengths and limitations of the study

The main strength of our study is that we show for the first time representation of event timing in the supra-second range in the cerebellum. In addition, we show behavioral relevance for such representations in reducing the latency to generate motor actions. We chose an innate reflex behavior, as opposed to behaviors invoking reward (Wagner et al., 2017; Kostadinov et al., 2019; Heffley and Hull, 2019) to eliminate confounds from reward-related mechanisms. Thus, the predictive and error-related activity we see in Purkinje cells drive sensory expectations and motor planning and likely perform an innate basic function in sensori-motor integration. Further,

we show that representations of timing are encoded in entrained rhythmic activity and in ramping activity, in support of models invoking such mechanisms in the neural representation of time (Gibbon, 1977; Simen et al., 2011).

The main limitation of our study is that we performed calcium imaging from partially immobilized larvae and electrophysiology from paralyzed larvae, thus reducing the repertoire of sensory signals that larvae would typically encounter in their environments. Nevertheless, previous studies show that strong visual feedback is sufficient to evoke optomotor responses similar to those seen in freely swimming larvae; the absence of sensori-motor feedback that normally accompanies free swimming does not seem to affect these responses severely (Ahrens et al., 2012; Mu et al., 2019; Portugues and Engert, 2011).

Ethological relevance of internal models of optic flow timing in larval zebrafish

Shallow water streams inhabited by larval zebrafish often show locally periodic changes in flow due to water waves or vortex streets shed by objects intercepting laminar flow. Fast and precise reactions to these perturbations caused by flowing water are likely to prevent fish from being washed away from a favorable environmental niche. Apart from being acquired rapidly, we show that the internal model is readily adaptive to sudden changes in periodicity (Figure 4G, H), making it highly relevant in the natural setting. In addition to this homeostatic function, it is possible that fish incorporate predicted environmental perturbations to fine tune other behavioral responses such as escape swims or prey capture maneuvers, such that the motor command generated in these situations compensates for displacement due to expected flow patterns.

Neural mechanisms underlying timing representations

Our results reveal activity in Purkinje cells that is entrained to the onset of periodic visual stimuli. In particular, we found three classes of cells: (i) those that were entrained to the flow stimulus but showed no response in the absence of flow and thus were purely flow responding; (ii) those that were entrained to the flow stimulus and showed modest but time-locked prediction error responses when flow was turned off; and (iii) those that were largely prediction error responding cells with absent to modest flow responses (Figure S6). Presence of these entrained flow responses and entrained PE responses indicate mechanisms to generate a rhythm that

synchronizes with an imposed periodic sensory stimulus. Similar entrained responses have been observed in tectal cells when larval zebrafish were presented visual stimuli periodic over several seconds (Sumbre et al., 2008). We found using loose patch recordings in Purkinje cells that the entrained flow responses could be due to both increased SS and CF rates that predictively ramp up even prior to onset of flow (Figure 5H-I). While SS can be modulated by increased synaptic input from granule cells, the CF rates suggest an increase in firing of the olivary neurons. Taken together with the study of Sumbre et al., we propose that predictive ramping and entrained representation of time intervals is distributed across multiple brain areas including the tectum, the inferior olive and the cerebellum. It is also likely that the entrained responses are fed to Purkinje cells from the tectum via granule cells.

Prediction error responses, observed in the third class of Purkinje cells, are due to a strong upregulation of CF inputs with little contribution due to SS modulation (Figure 5B-D). This indicates that the PE responses observed in Purkinje cells are mainly due to inputs from the inferior olive. The olivary input to Purkinje cells is typically regarded as a 'teaching' signal encoding errors in movements via their duration (Yang and Lisberger, 2014) and temporal distribution (Herzfeld et al., 2018; Suvrathan et al., 2016). Here, we have shown that olivary input to Purkinje cells also signals prediction errors in interval timing over many seconds, irrespective of generation of motor output (Figure 3). Evidence from human imaging studies and lesion studies in non-human primates supports a role for the olivo-cerebellar system in learning stimulus timing independent of motor performance (Ashe and Bushara, 2014).

Using an algorithmic model, we show that periodicities of sensory stimuli could be learnt via a simple learning rule that utilizes the sensory signal itself (F_{in}) and an internally generated model (E). Mismatches between the two lead to proportionate PE signals, which are then used to adjust the periodicity of E such that it quickly converges to F_{in} (Figure 8). In our experiments, we found neural correlates for F_{in} and predictive pre-flow ramps involved in motor planning in cluster 4 cells. On the other hand, in cells part of clusters 2,3,5,8, we found strong PE signals in probe trials and subdued but detectable calcium responses in non-probe trials, potentially corresponding to predictions of optic flow made by the internal model E. Since both predictions and prediction errors converge in this group of Purkinje cells, the learning rule for updating the

internal model is likely executed by them with inputs from the olive and from sensory areas. Cerebellar feedback potentially plays a key role in updating the timing representations present in these upstream sensory areas. The cerebellum is already demonstrated to perform such a function for the motor domain (Chabrol et al., 2019; Ebner, 2013; Gao et al., 2018; Wolpert et al., 1998), and with this study we propose an extension of this function to the supra-second temporal domain.

To summarize, we show how larval zebrafish acquire and use internal models of timing of optic flow in their environment to predictively modulate optomotor responses. These findings add a new dimension to our understanding of behavior generation algorithms employed by larval zebrafish. The role of the cerebellum and feedback loops formed with sensory areas of the brain are likely to be conserved across organisms and further investigation can provide mechanistic insight into the fundamental principles of how brains adaptively internalize rules of the world across a range of behaviorally relevant timescales.

Methods

Fish

We used 6-8 dpf zebrafish (*Danio rerio*) larvae for all experiments. The larvae were raised in E3 medium (composition in mM: 5 NaCl, 0.17 KCl, 0.33 CaCl2, 0.33 MgSO4, 0.5 methylene blue) at 28.5°C in accordance with standard protocols (https://zebrafish.org/home/guide.php). Tg(aldoca:GCaMP6s) ; nacre$^{-/-}$ larvae (from Prof. Masahiko Hibi, Nagoya University, Japan), outcrossed into the Indian wildtype (from local aquarium suppliers) background were used for experiments involving two-photon imaging. Indian wildtype larvae were used for electrophysiological recordings. All experimental procedures were approved by the Institutional Animal Ethics Committee of the National Centre for Biological Sciences.

Experimental preparation

For experiments involving two-photon imaging, 7-8 dpf zebrafish larvae were anaesthetized by briefly immersing them in 0.017% MS222 (Sigma-Aldrich) and embedded dorsal side up in a drop of 2% low gelling temperature agarose (Sigma-Aldrich) placed in the center of a 60mm petri dish lid. The dish was filled with E3 medium and the tail below the level of the swim

bladder was freed from agarose. The embedded fish were allowed to recover for 4-8 hours before the experiment.

Real-time motor output detection for closed-loop optomotor feedback

Custom Bonsai workflows (Lopes et al., 2015) were used for real-time motion detection. The algorithm used by our software for online motion detection closely matched previously published protocols (Ahrens et al., 2012; Portugues and Engert, 2011). Video based motion detection was done at 200 fps using a Flea3-USB3.0 camera (FLIR). The tail of the fish was illuminated from one side by a collimated 780nm LED (M780D2, Thorlabs) and imaged onto the camera sensor below (Figure 1A), using a reversed Nikon 50mm f/1.8d lens with a 24mm extension tube for increased magnification. Both the illumination and imaging light paths were filtered through 780nm bandpass filters (FBH-780-10, Thorlabs). The imaging light path was filtered to exclude light from the visual stimulus and two-photon laser and the illumination light path was filtered to block low intensity visible light emission from the 780nm LED. Real-time motion detection was performed by frame subtraction. The fraction of motion pixels in each frame, which scales with the amount of tail movement, was lowpass filtered with a 10ms time constant to obtain the instantaneous swim strength (ISS). This lowpass filter simulates the inertial effects experienced by larval fish in water. The ISS was streamed in real-time using Open Sound Control (OSC) protocol to custom software written in Processing 2.2.1 (https://processing.org/). This software generated visual stimulus, executed the experimental protocol, and generated TTL signals to synchronize two-photon imaging or electrophysiology data acquisition.

ISS for the electrophysiology preparation was estimated from fictive swims recorded unilaterally from the ventral root. Analog output from the recording amplifier was digitized at 12KHz in 10ms chunks (PCIe-6361, National Instruments) and acquired using a Bonsai workflow. Each 10ms chunk was bandpass filtered between 0.2-5kHz. The standard deviation of each chunk was calculated and the offset induced by recording noise was subtracted. This signal was lowpass filtered at 10Hz and thresholded manually to obtain an estimate of the ISS, which was streamed to the experiment control software.

The ISS was scaled individually for each fish to obtain a realistic estimate of swim velocity. 1-3 trials of optic flow at 10mm/s lasting 10-15s were presented before the start of each experiment in the open-loop configuration. A scaling factor, *s*, was calculated from these trials such that the ISS when scaled resulted in an average swim bout velocity of 15mm/s. This process is described by the following equation.

$$vswim_n = s \times g \times ISS_n$$

Where *n* is the frame count. *vswim* is the instantaneous velocity of the fish in the closed-loop environment. *s* is the scaling factor set individually for each fish. *g* is the gain of the closed-loop feedback, set at 1.0 for all experiments. *ISS* is the instantaneous swim strength.

Visual stimulus

Custom software written in Processing 2.2.1 was used to control the experimental protocol as well as to generate and update the visual stimulus at 120Hz. The visual stimulus consisted of square wave grating with a spatial period of 10mm presented 5mm beneath the fish. During optic flow-on phases, the grating drifted at 10mm/s in the tail to head direction. Motor output of the fish during the optic flow-on phases resulted in realistic deceleration and a smooth change in direction of optic flow based on the following equation.

$$vgrating_n = vflow_n - vswim_n$$

Where $vgrating_n$, $vflow_n$ and $vswim_n$ are the instantaneous velocities at frame *n* of the grating stimulus, externally imposed optic flow and the fish respectively.

In the calcium imaging setup, visual stimulus was projected on a 60mm diameter diffusive paper screen placed 5mm below the fish. The projector was custom built around a 5-inch LCD panel (Adafruit) removed from its housing. The LCD was illuminated from behind with a collimated 617nm LED (Luxeonstar) and was imaged onto the projection screen. A custom made driver was used to power the LED antiphase to the linescans of the fast x-galvo during two-photon imaging. This eliminated the possibility of bleedthrough of light from the visual stimulus into the calcium

imaging channel. In addition to this, a longpass filter (575lp, Chroma) was placed in the projection light path to prevent harmful levels of light from reaching the PMT. The final pixel size on the projection screen was 0.32mm. A 5X5mm window was cut out in the projection screen to facilitate video recording of tail movements from below. Visual stimulus for the electrophysiology experiments was presented directly on an LCD screen positioned beneath the fish.

Behavior assays

Fish were placed in a one-dimensional closed-loop optomotor track as described above. They were presented with repetitive trials of optic flow with a trial duration of 2s, which was kept constant for all experiments. The inter-trial-intervals (ITIs) were 5s long, unless specified otherwise. Gratings were stationary in the ITIs. 10% of trials chosen pseudorandomly were probe trials, in which optic flow was not presented (Figure 1B). The pseudorandom distribution was set such that one trial was chosen to be a probe trial for each 10 trial chunk of the experiment. Fish used for experiments were previously never exposed to rhythmic changes in optic flow. Each fish was presented with 100 trials. Only fish that were behaviorally responsive by generating at least 1 swim bout during the pre-experiment scaling process described above were put through the rest of the experimental protocol.

To test for underlying entrainment to the timing of optic flow, we presented each fish with a block of 20 consecutive trials with 5s ITIs, without probe trials, followed by 10 consecutive probe trials with the same 5s ITIs. Each fish was presented with 5 repeats of this trial structure (Figure 4A-F).

Adaptability of internal representations was tested by changing the ITI during the experiment (Figure 4G, H). In these experiments, fish were initially presented with 60 trials of optic flow with 5s ITI after which the interval was switched to 7s for another 60 trials, with no gap in between the two sets of 60 trials.

In electrophysiology experiments (Figure 5), fictive motor recordings were obtained from 9 out of 20 fish. Closed-loop feedback was provided for those fish and the remaining 11 fish went

through the experimental protocol without closed-loop feedback. Data from both groups were pooled together.

Two-photon calcium imaging

Head-restrained Tg(aldoca:GCaMP6s) ; nacre -/- larvae were used for all experiments. Imaging was performed on a custom two-photon microscope controlled using ScanImage 3.8 (Pologruto et al., 2003). A Ti-Sapphire laser (Chameleon Ultra II, Coherent) tuned to 920nm was used to excite GCaMP6s using a laser power of 20-30mW at the sample plane. The laser was focussed at the sample using a 20X 1.0NA objective lens (XLUMPLFLN20XW, Olympus), downstream of 50mm and 300mm focal length scan and tube lenses (AC-300-050B and AC-508-300-B, Thorlabs). Scanning was achieved using 3mm aperture scan mirrors (6215H, Cambridge Technology). A single 512X128 pixel field of view with 0.53µm pixel size, centred around the Purkinje cell layer was scanned using a pixel dwell time of 1.6µs, resulting in a frame rate of 7.8Hz. Fluorescence emission from GCaMP6s was bandpass filtered (FF01-520/70, Semrock) and detected with a GaAsP PMT (H7422PA-40, Hamamatsu). Output from the PMT was amplified using a preamplifier (SR570, Stanford Research Systems) and acquired using the same data acquisition card used to drive the scan mirrors (PCI-6110, National Instruments). Data acquisition from the microscope was triggered by a TTL pulse generated by an arduino connected to a separate computer running the behavior protocol. We acquired a continuous timeseries of two-photon images for each fish, spanning the duration of the experimental protocol.

Two-photon laser ablations

Tg(aldoca:GCaMP6s) ; nacre$^{-/-}$ larvae were prepared for cerebellum ablations using the same protocol as used for the calcium imaging experiments. 10 planes within the Purkinje cell layer, separated by 4µm, were serially scanned with the same scanning parameters used for the imaging experiments. Ablations were confined to the Purkinje cell layer using visual aid from GCaMP fluorescence. The laser was tuned to 920nm with a power of ~230mW at the sample plane. Each plane was scanned 10 times before moving to the next. This led to effective plasma mediated lesioning of the whole cerebellum within the region being scanned. Lesions were confirmed visually by an immediate increase in fluorescence intensity due to uncontrolled influx of calcium

into the cytosol, followed by blebbing and disintegration of cells. Fish were allowed to recover for 1 hour post lesion before initiating the behavior protocol. The cerebellum was scanned while the behavior protocol was carried out, with laser power and scan settings identical to those used for calcium imaging in non-lesioned fish to maintain experimental conditions.

Electrophysiology

6-7dpf zebrafish larvae were first anesthetized in 0.01% MS-222 and transferred to a recording chamber. Two pieces of fine tungsten wire (California Fine Wire) were used to pin the larvae through the notochord onto a Sylgard (Dow Corning) slab in the recording chamber. A third pin was used to orient the head dorsal side up (Figure 5A). The MS-222 was then replaced by external solution (composition in mM: 134 NaCl, 2.9 KCl, 1.2 $MgCl_2$, 10 HEPES, 10 glucose, 2.1 $CaCl_2$, 0.01 d-tubocurarine; pH 7.8; 290 mOsm) and the skin covering the brain and along the tail was carefully removed using forceps (Fine Science Tools). The preparation was then taken to a rig apparatus.

Patch pipettes for loose patch recordings were made using thick-walled borosilicate capillaries (1.5 mm OD; 0.86 mm ID, Warner Instruments) and pulled to 1-1.5 μm tip diameter using a Flaming Brown P-97 pipette puller (Sutter Instruments), such that their resistance when backfilled with external solution was approximately 7-10 MΩ. Similarly, suction recording pipettes for fictive motor recordings were made using thin-walled borosilicate capillaries (1.5mm OD; 1.1mm ID, Sutter Instruments), pulled to ~5 μm tip diameter, such that their resistance when backfilled with external solution was ~0.7-1.5 MΩ.

First, ventral root recordings to monitor fictive swimming were obtained by guiding the pipette to a myotomal boundary (~15-20th somite) and applying mild suction. Once a successful recording was obtained, the focus was shifted to the cerebellum and loose patch recordings from Purkinje neurons were obtained. The pipettes were guided visually using the 60x/1.0NA water immersion objective of a compound microscope (Ni-E, Nikon) and a motorized micromanipulator (PatchStar, Scientifica). Once both recordings were obtained, the condenser of the microscope was gently moved to allow the introduction of a 5-inch LCD screen (Adafruit) to present visual stimuli. Recordings were included for analysis only if their quality did not deteriorate before at least 5 probe trials were presented.

Visual stimulus presentation and electrophysiological recordings were triggered simultaneously and acquired using a Multiclamp 700B amplifier, Digidata 1440A digitizer and pCLAMP software (Molecular Devices). The data were low-pass filtered at 2kHz using a Bessel filter and sampled at 50kHz at a gain between 10-2000, adjusted depending on the quality of each recording. The ventral root recordings were parallely acquired and real-time analysis was performed to provide closed-loop optomotor feedback as described above.

Data processing and analysis

Data processing and analysis was done primarily using Python (python.org). Both Python and MATLAB (Mathworks) were used for analysis of electrophysiology data.

Behavior data processing

Swim velocity data and timestamps saved from the experiment control software at ~120Hz were used for estimating latency (Figure 1b). A simple threshold was sufficient to detect the beginning and end of swim bouts as signal to noise ratios were sufficiently high.

Latency modulation around probe trials

Latency modulation around probe trials was estimated by determining the fold change in latency relative to baseline latency in each trial for a 10 trial window around a probe trial (Figure 6 A, B, D). The baseline was determined as the mean latency observed over 5 trials before the probe trial. This normalization was necessary as slow drifts in latency developed over the duration of the experiment. Trials were selected if there were at least 3 swim bouts on either side of the probe trial. A minimum of 3 such trials were required per fish to obtain an average latency modulation trace for that fish. These criteria were pre-selected before the analysis was performed and the statistical inference did not change when we later varied the selection criteria to include probe trials with at least 1 swim bout on either side. 17 non-lesioned fish (Figure 6B) and 11 cerebellum-lesioned fish (Figure 6D) passed these exclusion criteria.

Calcium trace extraction

Calcium traces were extracted from individual Purkinje cell somata using a semi-automated processing pipeline written in Python (Figure S1). The images were corrected for translation along the X-Y plane using phase correlation with the registration module in scikit-image (Walt et al., 2014). After motion correction, the centres of individual cells were identified manually using a GUI. A three layer neural network trained using a subset of data from these experiments was used to mark cell boundaries, guided by the manually identified centre coordinates. Pixels within the ROI were averaged to obtain fluorescence intensity of each cell for a given frame. Fold change in fluorescence intensity over baseline (dF/F) was calculated with baseline estimated as the tenth percentile of a one minute window around each frame. Overlapping pixels assigned to more than one ROI were excluded from any of the assigned ROIs to avoid signal contamination from neighbouring cells. The resultant ROIs consisted of 140 ± 26 (mean ± SD) pixels each.

Hierarchical clustering

Correlation based hierarchical clustering was used to group cells based on functional response types. 1874 cells from 27 fish were pooled for clustering. This clustering step was done separately for optic flow and probe triggered average responses of all cells. The number of clusters was determined by a threshold for linkage distance between clusters. This threshold was chosen manually from a dendrogram and was consistent with automated estimation using elbow plots. 3 functional clusters each were found for both optic flow and probe triggered responses. We then subdivided clusters by finding the intersections of each of the optic flow and probe response clusters, resulting in a total of 9 potential clusters based on both optic flow and probe response properties. Any cell with a Pearson's correlation coefficient less than 0.3 with the mean response profile of that cluster was excluded from the cluster. Out of these 9 potential clusters, 4 were disregarded from further analysis as the number of cells averaged less than 1 per fish. Cluster numbers 2, 3, 4, 5 and 8 were taken for further analysis and contained 175, 175, 954, 179 and 90 cells respectively.

Due to the short 2s duration of each trial, motor responses could not be reliably distinguished from optic flow responses in the triggered average traces. Cells involved in motor command generation will be classified by this method as optic flow responsive due to the high correlation between optic flow and motor output.

Estimation of PE response probability and amplitude

For analyses involving single trial estimation of PE responses, calcium traces without trial averaging were evaluated for a significant increase in fluorescence in probe trials. A response was considered significant if the mean fluorescence intensity of a 1s window centered around the end of a probe trial was greater than the mean fluorescence intensity of the 1s window preceding the onset of that probe trial by at least 3 SDs of the pre-trial levels. The average dF/F of the 1s window around the end of a probe trial is referred to as the PE response amplitude. The number of probe trials in Figure 2F, G is greater than 10 since we presented multiple groups of fish with different sets of 10 pseudo randomly chosen trials as probe trials (3 groups of 5, 7 and 15 fish).

Both PE response probability and amplitude were calculated for individual probe trials across cells and for individual cells across all probe trials. These can be distinguished by the labels 'Trial-wise' or 'Mean' PE probability/amplitude respectively in the figures. In all cases, error bars represent variability across fish as described in the figure legends.

Analysis of PE response onset

Onset times were estimated using the average response profile of the signal of interest for each fish. The onset time was determined as the time point of maximum slope, where the slope was estimated for each time point with respect to the value 5 calcium imaging frames in the future. A randomization-based test was used to determine whether the variance of the onset time distribution across fish is significantly lower than expected by drawing random samples of equivalent sample size from a uniform distribution (Kim et al., 2019). P-values were estimated from the number of times, out of 10^6 runs, the variance of random samples was lower than the variance of the onset time distribution. A significantly lower variance indicates temporal specificity of response onsets.

Spike detection and analysis

Spikes were identified as events that showed large fluctuations relative to a 25ms rolling window baseline and the peak times and amplitudes were extracted. Small amplitude events were classified as simple spikes (SSs) and large amplitude events as climbing fiber (CF) inputs

(Sengupta and Thirumalai, 2015). Once identified and sorted, recordings were triggered to the start of optic flow trials or probe trials. Mean firing rates for optic flow and probe trials were estimated by convolving peri-event time histograms of 20ms binwidth with a 200ms gaussian kernel. Analysis was done using custom scripts written in Python. CF/SS event detection was done in MATLAB (https://github.com/wagenadl/mbl-nsb-toolbox).

Modulation indices were calculated for each kind of event (CF and SS) using the following formula:

$$\text{modulation index} = \frac{\text{mean event rate} - \text{mean baseline event rate}}{\text{mean event rate} + \text{mean baseline event rate}}$$

Where the mean event rate is the mean CF or SS rate during the 2s trial period and the mean baseline event rate is the mean event rate in the 2s window prior to trial onset. The modulation index has a range of -1 to 1 with positive values for an increase in event rate during a trial compared to baseline and negative values for a reduction in event rate.

Analysis of event rate modulation in probe trials

Each cell was evaluated independently for a significant increase in CF or SS event rates during probe trials. We randomly sub-sampled trials from non-probe trials 1000 times and estimated the mean baseline event rates for each sub-sampled group of trials. The number of sub-sampled trials in each group was equal to the number of probe trials for that cell. The distribution generated by repeated sub-sampling gives us an estimate of the inherent variability in event rate estimates when trial counts are low, as is the case for probe trials. If the mean event rate during probe trials was greater than the mean + 2 SD of the random, sub-sampled distribution, the increase was considered significant.

Algorithmic modeling

The algorithmic model was implemented in Python as described here and in the results section and simulations were carried out with a time step of 0.01s.

Optic flow input (F_{in}) was similar to what we used in the experiments. 0 when optic flow is off, 1 when optic flow is on. The duration of each optic flow-on trial was always 2s. The inter-trial interval (ITI) and the placement of probe trials was varied as mentioned in the results section.

Based on our experimental observations, we assumed the presence of an entrained internal model (E) which generated 2s long bursts with a dynamic inter-burst interval (IBI). A learning rule tuned the IBI based on PE feedback as described below to adaptively learn stimulus timing. E takes a value of 0 during the IBIs and 1 during bursts.

To model PE signals, we estimated the phase shift between E and F_{in}. This was done for each time step by subtracting the optic flow input (F_{in}) from E. Since a simple subtraction would result in paired PE signals with opposite signs that cancel out each other on average, we implemented a refractory period of 2s which began when PE returned back to zero or changed sign after attaining a non-zero value. During this refractory period PE was set to zero. This ensures that when there is a phase shift between E and F_{in}, its direction is encoded by the sign of the PE signal and magnitude is encoded by the duration of the PE signal (Figure 8D, top).

At each time point t, the inter-burst interval (IBI) of E was updated using the learning rule:

$$IBI(t + dt) = IBI(t) + \alpha \times PE(t)$$

where $\alpha = 0.04$, is the learning rate.

Locomotor drive M was modeled using the following equation and swim bouts were triggered when M reached a threshold of 0.275. This threshold was chosen to generate realistic swim latencies of ~1.2s. After reaching the threshold, M was reset to zero for a refractory period of 0.2s to mimic realistic swim bout intervals seen in fish (Bahl and Engert, 2020).

$$\tau_m \frac{dM}{dt} = -M(t) + F_{in}(t) - 0.2 \times |PE(t)|$$

τ_m of 4s was used to mimic integration times for swim decisions (Bahl and Engert, 2020).

Model convergence

Time to converge was determined as the first instance where the predicted time interval encoded in IBI fell below and remained within 10% of the stimulus interval for a period of 5 trials. These times are indicated by the arrows in Figure 8D.

Statistics

All tests were performed in Python using SciPy (Virtanen et al., 2020) and Statsmodels (Seabold and Perktold, 2010). The statistical tests used and their results are mentioned in the figure legends. In cases where linear mixed-effects models were used, we selected either random intercept or random intercept and slope models, based on which one of the two models resulted in a better fit as indicated by a higher log-likelihood value. In all cases, linear mixed-effects models were used to evaluate the significance of slope.

Supplementary Video 1

Average calcium responses of representative cells from the same fish across 5 trial aligned epochs of the experimental protocol shown in Figure 1b. Dark blue traces show cells responsive to optic flow and cyan traces highlight cells with strong probe responses. Dashed red line marks probe onset.

Supplementary Video 2

Entrained PE responses in a representative fish. Top panel shows raw fluorescence of Purkinje cells averaged over 5 stimulus blocks. Plots show individual dF/F traces (cyan) and their average (yellow) for the 13 cells indicated by yellow arrowheads in the top panel. Bottom-most trace represents the optic flow stimulus. Purple dashed lines indicate the positions of successive probe trials.

References

Ahrens, M.B., Li, J.M., Orger, M.B., Robson, D.N., Schier, A.F., Engert, F., and Portugues, R. (2012). Brain-wide neuronal dynamics during motor adaptation in zebrafish. Nature *485*, 471–477.

Antinucci, P., Folgueira, M., and Bianco, I.H. (2019). Pretectal neurons control hunting behaviour. ELife *8*, e48114.

Ashe, J., and Bushara, K. (2014). The Olivo-Cerebellar System as a Neural Clock. In Neurobiology of Interval Timing, H. Merchant, and V. de Lafuente, eds. (New York, NY: Springer), pp. 155–165.

Bae, Y.-K., Kani, S., Shimizu, T., Tanabe, K., Nojima, H., Kimura, Y., Higashijima, S., and Hibi, M. (2009). Anatomy of zebrafish cerebellum and screen for mutations affecting its development. Dev. Biol. *330*, 406–426.

Bahl, A., and Engert, F. (2020). Neural circuits for evidence accumulation and decision making in larval zebrafish. Nat Neurosci *23*, 94–102.

Bell, C.C., Han, V., and Sawtell, N.B. (2008). Cerebellum-like structures and their implications for cerebellar function. Annu. Rev. Neurosci. *31*, 1–24.

Buhusi, C.V., and Meck, W.H. (2005). What makes us tick? Functional and neural mechanisms of interval timing. Nat Rev Neurosci *6*, 755–765.

Buonomano, D.V. (2007). The biology of time across different scales. Nat Chem Biol *3*, 594–597.

Chabrol, F.P., Blot, A., and Mrsic-Flogel, T.D. (2019). Cerebellar Contribution to Preparatory Activity in Motor Neocortex. Neuron *103*, 506-519.e4.

Chen, T.-W., Wardill, T.J., Sun, Y., Pulver, S.R., Renninger, S.L., Baohan, A., Schreiter, E.R., Kerr, R.A., Orger, M.B., Jayaraman, V., et al. (2013). Ultrasensitive fluorescent proteins for imaging neuronal activity. Nature *499*, 295–300.

Ebner, T.J. (2013). Cerebellum and Internal Models. In Handbook of the Cerebellum and Cerebellar Disorders, M. Manto, J.D. Schmahmann, F. Rossi, D.L. Gruol, and N. Koibuchi, eds. (Dordrecht: Springer Netherlands), pp. 1279–1295.

Gao, Z., Davis, C., Thomas, A.M., Economo, M.N., Abrego, A.M., Svoboda, K., Zeeuw, C.I.D., and Li, N. (2018). A cortico-cerebellar loop for motor planning. Nature 1.

Gibbon, J.H. (1977). Scalar expectancy theory and Weber's law in animal timing. Psychological Review.

Giovannucci, A., Badura, A., Deverett, B., Najafi, F., Pereira, T.D., Gao, Z., Ozden, I., Kloth, A.D., Pnevmatikakis, E., Paninski, L., et al. (2017). Cerebellar granule cells acquire a widespread predictive feedback signal during motor learning. Nature Neuroscience *20*, 727–734.

Hamling, K.R., Tobias, Z.J.C., and Weissman, T.A. (2015). Mapping the development of cerebellar Purkinje cells in zebrafish. Dev Neurobiol *75*, 1174–1188.

Heffley, W., and Hull, C. (2019). Classical conditioning drives learned reward prediction signals in climbing fibers across the lateral cerebellum. ELife *8*, e46764.

Herzfeld, D.J., Kojima, Y., Soetedjo, R., and Shadmehr, R. (2018). Encoding of error and learning to correct that error by the Purkinje cells of the cerebellum. Nature Neuroscience *21*, 736.

Ivry, R.B., and Keele, S.W. (1989). Timing Functions of The Cerebellum. Journal of Cognitive Neuroscience *1*, 136–152.

Jeffress, L.A. (1948). A place theory of sound localization. Journal of Comparative and Physiological Psychology *41*, 35–39.

Jha, U., and Thirumalai, V. (2020). Neuromodulatory Selection of Motor Neuron Recruitment Patterns in a Visuomotor Behavior Increases Speed. Curr. Biol. *30*, 788-801.e3.

Karmarkar, U.R., and Buonomano, D.V. (2007). Timing in the Absence of Clocks: Encoding Time in Neural Network States. Neuron *53*, 427–438.

Kim, S.S., Hermundstad, A.M., Romani, S., Abbott, L.F., and Jayaraman, V. (2019). Generation of stable heading representations in diverse visual scenes. Nature *576*, 126–131.

Kitamura, K., and Häusser, M. (2011). Dendritic calcium signaling triggered by spontaneous and sensory-evoked climbing fiber input to cerebellar Purkinje cells in vivo. J. Neurosci. *31*, 10847–10858.

Knogler, L.D., Markov, D.A., Dragomir, E.I., Štih, V., and Portugues, R. (2017). Sensorimotor Representations in Cerebellar Granule Cells in Larval Zebrafish Are Dense, Spatially Organized, and Non-temporally Patterned. Current Biology *27*, 1288–1302.

Knogler, L.D., Kist, A.M., and Portugues, R. (2019). Motor context dominates output from purkinje cell functional regions during reflexive visuomotor behaviours. ELife *8*, e42138.

Koekkoek, S.K.E., Hulscher, H.C., Dortland, B.R., Hensbroek, R.A., Elgersma, Y., Ruigrok, T.J.H., and De Zeeuw, C.I. (2003). Cerebellar LTD and Learning-Dependent Timing of Conditioned Eyelid Responses. Science *301*, 1736–1739.

Kostadinov, D., Beau, M., Blanco-Pozo, M., and Häusser, M. (2019). Predictive and reactive reward signals conveyed by climbing fiber inputs to cerebellar Purkinje cells. Nat Neurosci *22*, 950–962.

Kunimatsu, J., Suzuki, T.W., Ohmae, S., and Tanaka, M. (2018). Different contributions of preparatory activity in the basal ganglia and cerebellum for self-timing. ELife *7*, e35676.

Lewis, P.A., and Miall, R.C. (2003a). Brain activation patterns during measurement of sub- and supra-second intervals. Neuropsychologia *41*, 1583–1592.

Lewis, P.A., and Miall, R.C. (2003b). Distinct systems for automatic and cognitively controlled time measurement: evidence from neuroimaging. Current Opinion in Neurobiology *13*, 250–255.

Lopes, G., Bonacchi, N., Frazão, J., Neto, J.P., Atallah, B.V., Soares, S., Moreira, L., Matias, S., Itskov, P.M., Correia, P.A., et al. (2015). Bonsai: an event-based framework for processing and controlling data streams. Frontiers in Neuroinformatics *9*, 7.

Malapani, C., Rakitin, B., Levy, R., Meck, W.H., Deweer, B., Dubois, B., and Gibbon, J. (1998a). Coupled Temporal Memories in Parkinson's Disease: A Dopamine-Related Dysfunction. Journal of Cognitive Neuroscience *10*, 316–331.

Malapani, C., Dubois, B., Rancurel, G., and Gibbon, J. (1998b). Cerebellar dysfunctions of temporal processing in the seconds range in humans. NeuroReport *9*, 3907–3912.

Mauk, M.D., and Buonomano, D.V. (2004). The Neural Basis of Temporal Processing. Annual Review of Neuroscience *27*, 307–340.

McCormick, D.A., and Thompson, R.F. (1984). Cerebellum: essential involvement in the classically conditioned eyelid response. Science *223*, 296–299.

Medina, J.F., Garcia, K.S., Nores, W.L., Taylor, N.M., and Mauk, M.D. (2000). Timing Mechanisms in the Cerebellum: Testing Predictions of a Large-Scale Computer Simulation. J. Neurosci. *20*, 5516–5525.

Merchant, H., and de Lafuente, V. (2014). Introduction to the Neurobiology of Interval Timing. In Neurobiology of Interval Timing, H. Merchant, and V. de Lafuente, eds. (New York, NY: Springer), pp. 1–13.

Miall, C. (1989). The Storage of Time Intervals Using Oscillating Neurons. Neural Computation *1*, 359–371.

Miri, A., Daie, K., Burdine, R.D., Aksay, E., and Tank, D.W. (2011). Regression-Based Identification of Behavior-Encoding Neurons During Large-Scale Optical Imaging of Neural Activity at Cellular Resolution. Journal of Neurophysiology *105*, 964–980.

Mu, Y., Bennett, D.V., Rubinov, M., Narayan, S., Yang, C.-T., Tanimoto, M., Mensh, B.D., Looger, L.L., and Ahrens, M.B. (2019). Glia Accumulate Evidence that Actions Are Futile and Suppress Unsuccessful Behavior. Cell *178*, 27-43.e19.

Neuhauss, S.C.F., Biehlmaier, O., Seeliger, M.W., Das, T., Kohler, K., Harris, W.A., and Baier, H. (1999). Genetic Disorders of Vision Revealed by a Behavioral Screen of 400 Essential Loci in Zebrafish. J. Neurosci. *19*, 8603–8615.

Ohmae, S., Kunimatsu, J., and Tanaka, M. (2017). Cerebellar Roles in Self-Timing for Sub- and Supra-Second Intervals. J. Neurosci. *37*, 3511–3522.

Orger, M.B., Smear, M.C., Anstis, S.M., and Baier, H. (2000). Perception of Fourier and non-Fourier motion by larval zebrafish. Nat Neurosci *3*, 1128–1133.

Paton, J.J., and Buonomano, D. (2018). The Neural Basis of Timing: Distributed Mechanisms for Diverse Functions. Neuron.

Pologruto, T.A., Sabatini, B.L., and Svoboda, K. (2003). ScanImage: Flexible software for operating laser scanning microscopes. BioMedical Engineering OnLine *2*, 13.

Portugues, R., and Engert, F. (2011). Adaptive locomotor behavior in larval zebrafish. Front Syst Neurosci *5*, 72.

Rosbash, M., and Hall, J.C. (1989). The molecular biology of circadian rhythms. Neuron *3*, 387–398.

Seabold, S., and Perktold, J. (2010). Statsmodels: Econometric and Statistical Modeling with Python. Proceedings of the 9th Python in Science Conference 92–96.

Sengupta, M. (2015). Purkinje neurons in action: From single cells to ensembles. Tata Institute of Fundamental Research.

Sengupta, M., and Thirumalai, V. (2015). AMPA receptor mediated synaptic excitation drives state-dependent bursting in Purkinje neurons of zebrafish larvae. Elife *4*.

Simen, P., Balci, F., deSouza, L., Cohen, J.D., and Holmes, P. (2011). A Model of Interval Timing by Neural Integration. J. Neurosci. *31*, 9238–9253.

Spencer, R.M.C., and Ivry, R.B. (2013). Cerebellum and Timing. In Handbook of the Cerebellum and Cerebellar Disorders, M. Manto, J.D. Schmahmann, F. Rossi, D.L. Gruol, and N. Koibuchi, eds. (Dordrecht: Springer Netherlands), pp. 1201–1219.

Sumbre, G., Muto, A., Baier, H., and Poo, M. (2008). Entrained rhythmic activities of neuronal ensembles as perceptual memory of time interval. Nature *456*, 102–106.

Suvrathan, A., Payne, H.L., and Raymond, J.L. (2016). Timing Rules for Synaptic Plasticity Matched to Behavioral Function. Neuron *92*, 959–967.

Virtanen, P., Gommers, R., Oliphant, T.E., Haberland, M., Reddy, T., Cournapeau, D., Burovski, E., Peterson, P., Weckesser, W., Bright, J., et al. (2020). SciPy 1.0: fundamental algorithms for scientific computing in Python. Nat Methods *17*, 261–272.

Wagner, M.J., Kim, T.H., Savall, J., Schnitzer, M.J., and Luo, L. (2017). Cerebellar granule cells encode the expectation of reward. Nature *544*, 96–100.

Walt, S. van der, Schönberger, J.L., Nunez-Iglesias, J., Boulogne, F., Warner, J.D., Yager, N., Gouillart, E., and Yu, T. (2014). scikit-image: image processing in Python. PeerJ *2*, e453.

Wolpert, D.M., Miall, R.C., and Kawato, M. (1998). Internal models in the cerebellum. Trends in Cognitive Sciences *2*, 338–347.

Yang, Y., and Lisberger, S.G. (2014). Purkinje-cell plasticity and cerebellar motor learning are graded by complex-spike duration. Nature *510*, 529–532.

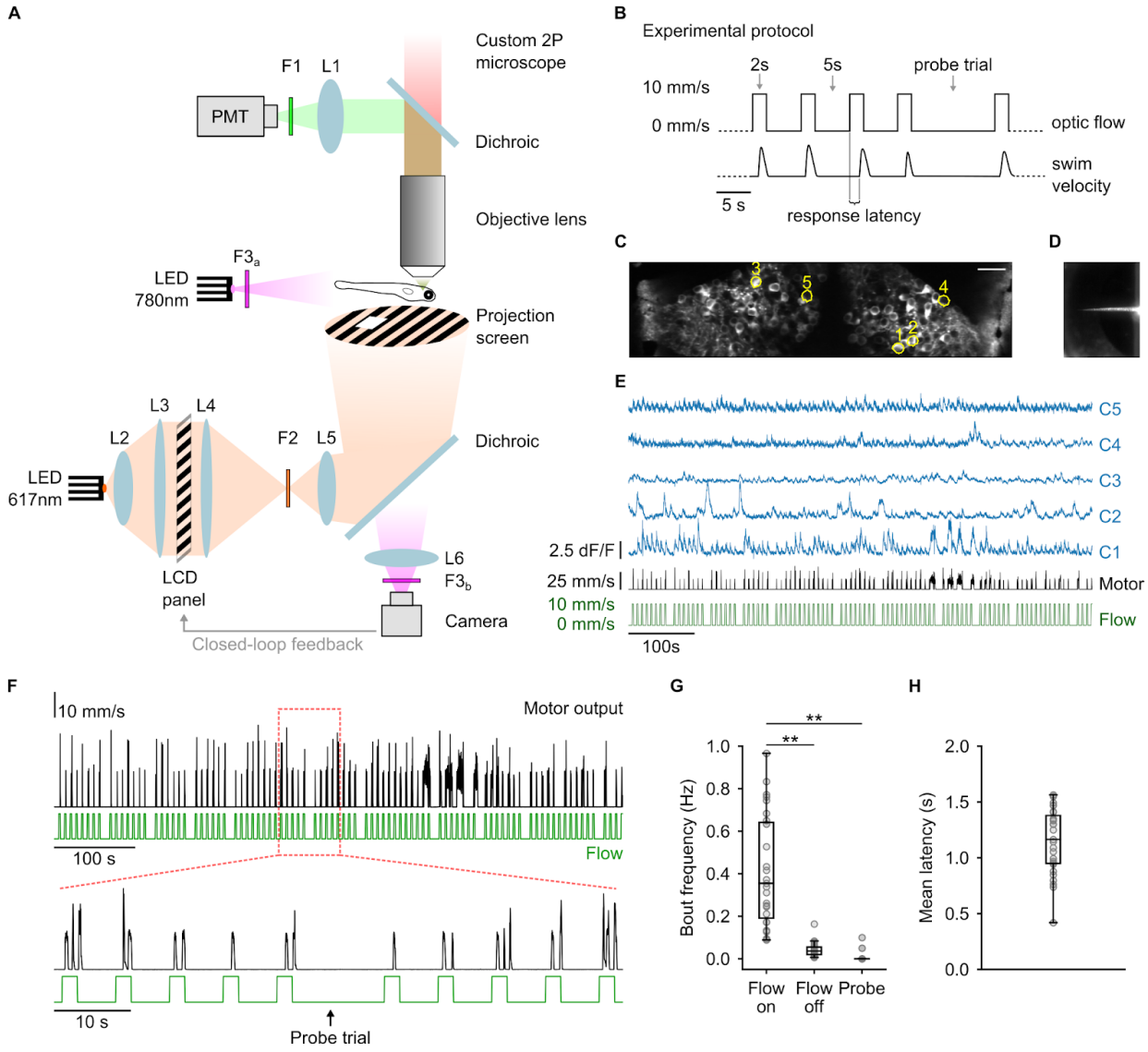

Figure 1. An interval timing task for larval zebrafish

(A) Schematic of the custom built experimental setup. A head restrained 7dpf zebrafish larva is placed in a closed-loop optomotor track underneath a two-photon microscope. L1-6: convex lenses, F1-3 optical filters (See Methods). (B) A cartoon of the experimental protocol. Each trial is 2s long followed by a 5s inter-trial interval. 10% of trials chosen pseudorandomly are probe trials in which optic flow is not turned on. Latency to respond to optic flow in each trial is measured as the behavioral readout. (C) Average image of a single optical plane of Purkinje cells specifically expressing GCaMP6s under the *aldoca* promoter. Scale bar: 20µm. (D) A video grab from the closed-loop camera showing the tail of a head restrained fish while two-photon imaging was being carried out. (E) Example calcium imaging traces (blue) from 5 cells (ROIs marked in (C)) aligned to motor output (black trace) and the optic flow stimulus (green trace). (F) Representative behavioral response during a 100-trial experiment (top) and a zoomed-in section showing swim bouts around a single probe trial (bottom). (G) Most swim bouts occur during optic flow presentation. Almost no swim bouts occur during probe trials or in the interval between trials. $p = 1.01 \times 10^{-13}$ by one-way repeated measures ANOVA, 27 fish. **p = 0.001 by Tukey's post hoc test. (H) Average latency distribution for 27 fish (1.15 ± 0.29, mean ± SD).

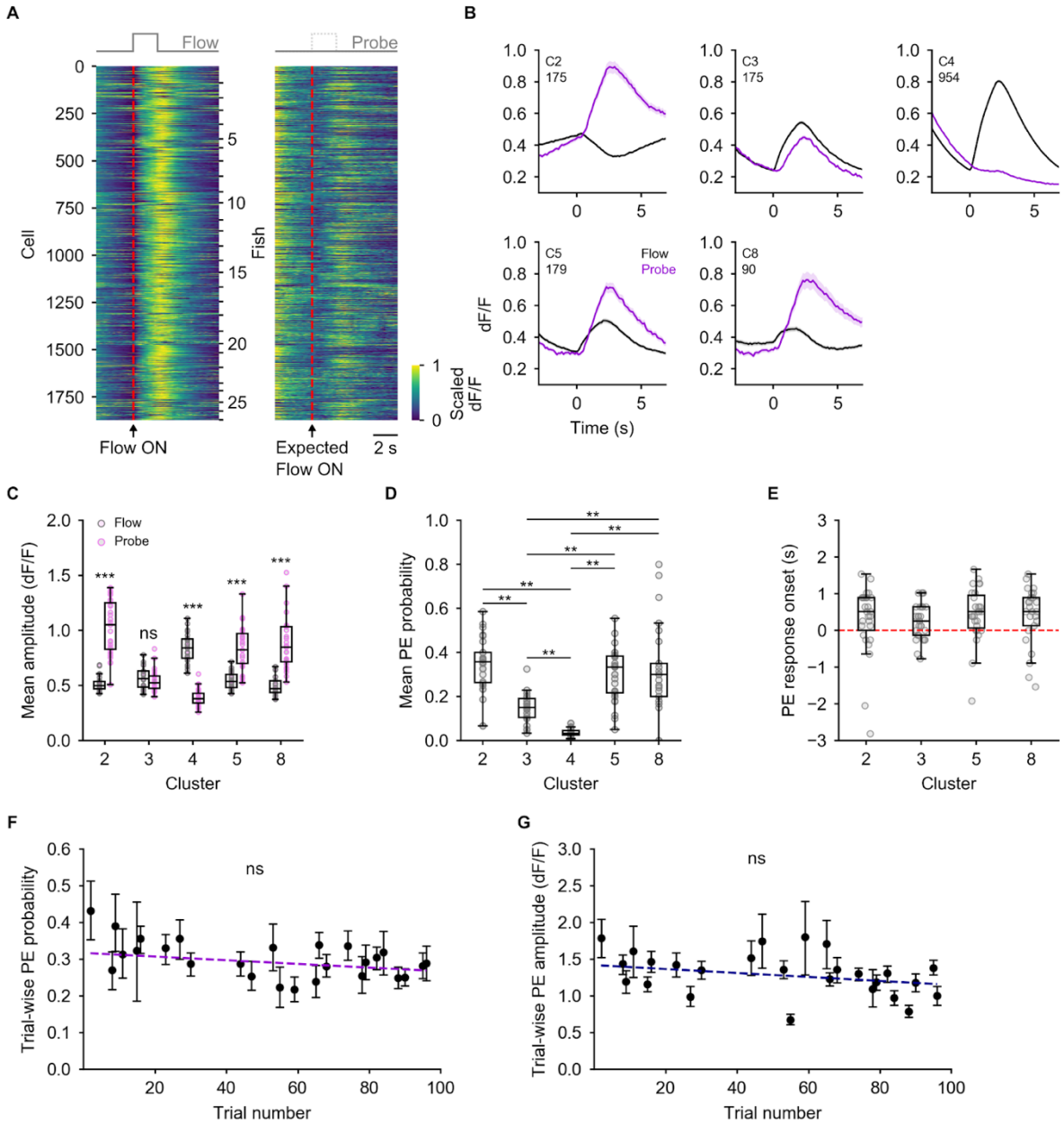

Figure 2. Purkinje cells encode a time-locked prediction error (PE) signal
(A) Optic flow and probe triggered average responses of all 1874 cells recorded from 27 fish. Each cell is normalized to a range of 0 to 1, representing its min and max dF/F. A widespread response to optic flow and to the expected time of onset of optic flow is noticeable across the population. (B) Cells grouped into 5 functional clusters by correlation based hierarchical clustering. Clusters 2, 3, 5 and 8 show large responses tuned to the onset of probe trials and weaker or no response during non-probe trials. Cells in cluster 4 do not show a response during probe trials but show large responses in non-probe trials caused by sensory and/or motor activity. Inset numbers show the number of cells in each cluster. Shaded regions represent SEM across cells in each cluster. (C) Clusterwise comparison of the amplitude of the probe and flow triggered average responses. Clusters 2, 5 and 8 show significantly larger responses in probe trials. ***$p < 0.001$ by paired t-test, 27 fish. (D) Average probability of a calcium response occurring in a given cell in a single probe trial. $p = 1.15 \times 10^{-18}$ by one-way ANOVA, 27 fish, **$p < 0.01$ by Tukey's post hoc test. (E) Time of onset of a calcium response during probe trials relative to the expected onset of optic

flow. The probe response is time-locked to the expected onset time of optic flow (statistics in Supplementary Table 1). Dashed red line at t = 0s indicates probe onset. Data points in panels (C-E) represent individual fish. (F, G) PE response probability and amplitude do not change significantly with trials, p = 0.988 and 0.985 respectively by linear mixed-effects.

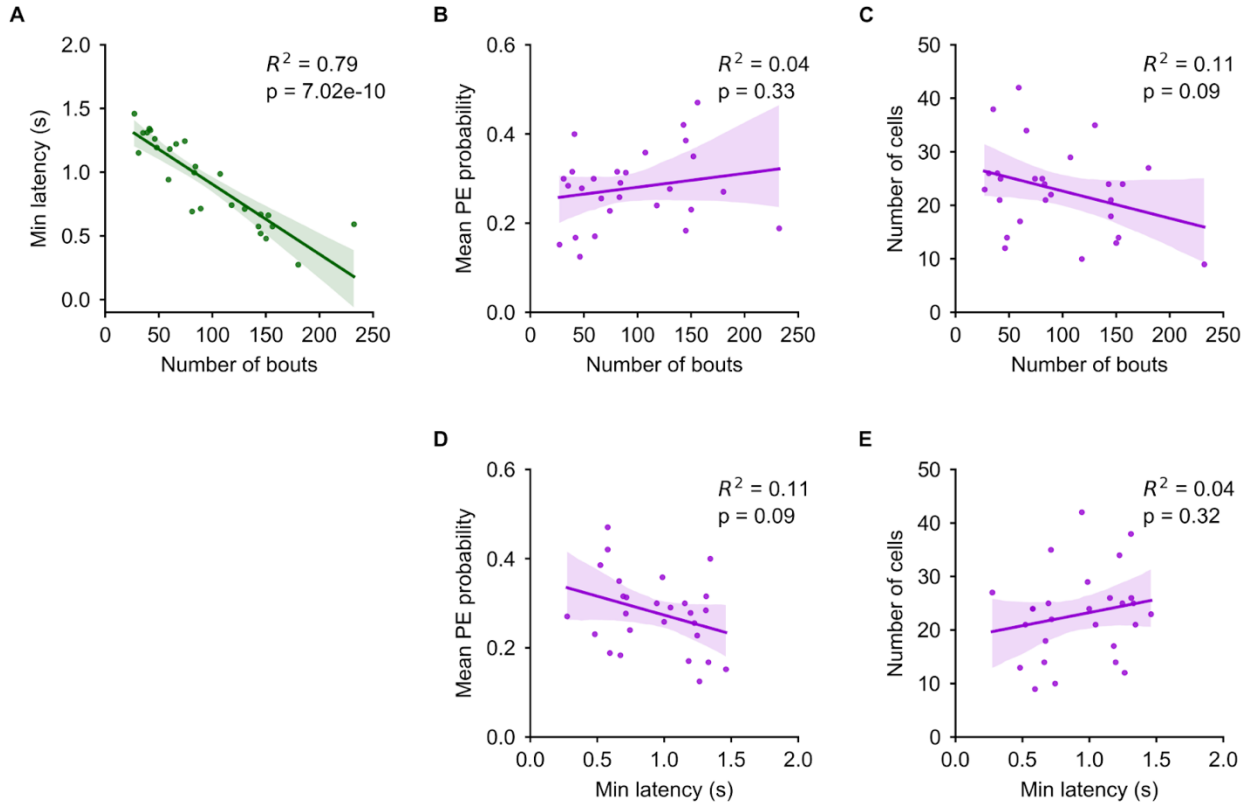

Figure 3. Purkinje cells encoding PE signals perform a motor-independent timing function
(A) Latency to swim in response to optic flow is strongly anti-correlated with the total number of swim bouts over 100 trials. (B, D) Mean PE response probability of cells in the probe-responsive clusters is not correlated with the number of swim bouts (B) or minimum latency (D). (C, E) The total number of probe responsive Purkinje cells does not depend on the number of swim bouts (C) or minimum latency (E). Individual data points represent fish (n = 27), solid lines are linear regression fits and shaded regions show 95% confidence intervals. p-values from Wald test for non-zero slope and R^2 for the fits are inset in each plot.

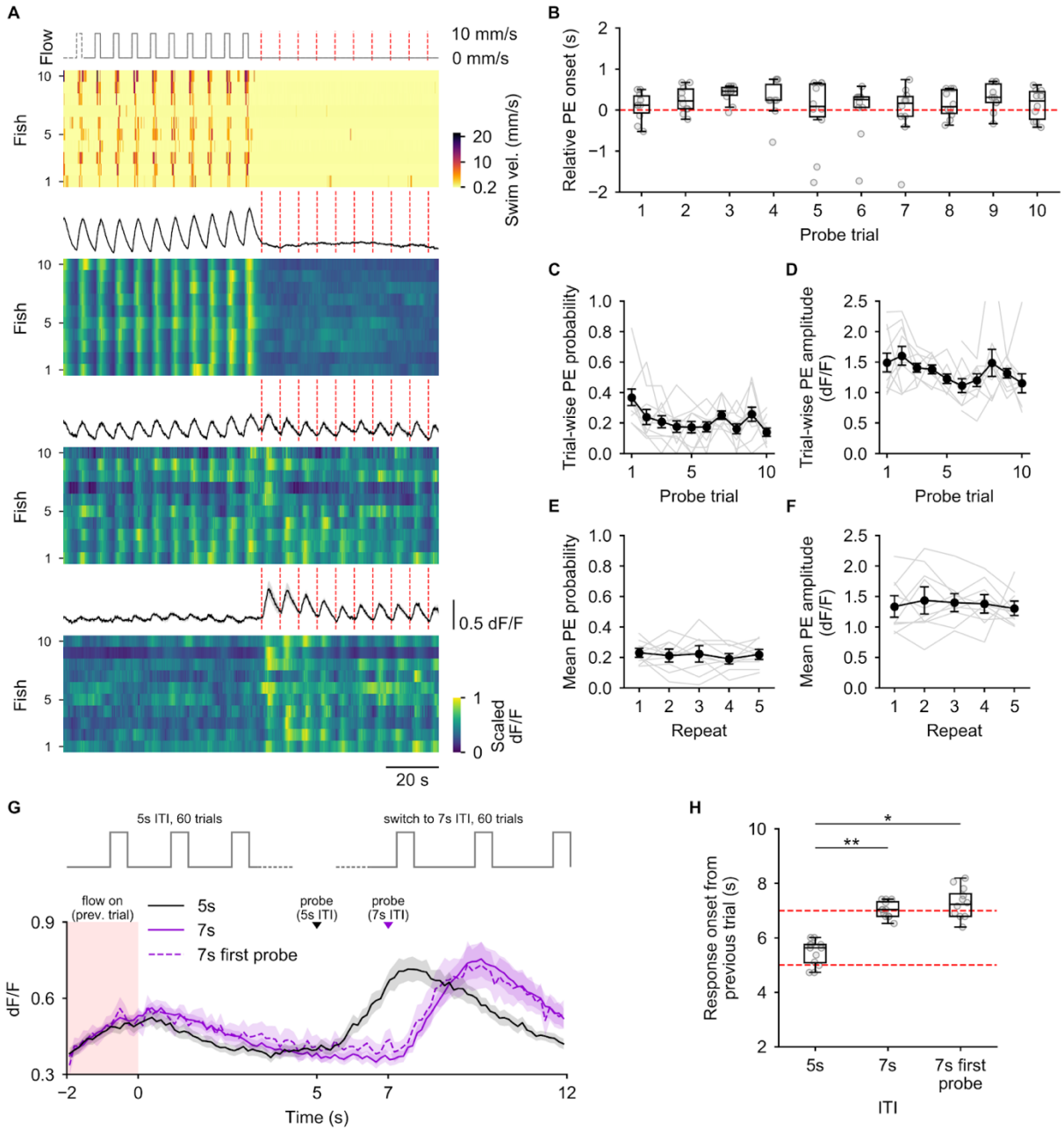

Figure 4. Optic flow timing is encoded in entrained neural activity and is adaptable
(A) Top panel: Average swim velocity of 10 fish aligned to the optic flow stimulus. Bottom three panels: Average responses of cells classified as optic flow responsive, entrained, or PE, based on correlation with regressors. Shaded regions around calcium traces represent SEM across 10 fish. (B) Onset times of the PE signal for cells in the bottom panel in (A), measured relative to the start of a probe trial for each of the 10 consecutive probe trials. Dashed red line indicates probe onset (t = 0s) (statistics in Supplementary Table 2). (C, D) Trial-wise PE response probability and amplitude for the 10 consecutive probe trials. (E, F) No change in mean PE response probability or amplitude was observed over the 5 repeats of the stimulus protocol. Error bars in (C-F) represent SEM across 10 fish. (G) Average response of the same cells during probe trials at 5s ITI (black) and 7s ITI (purple). Arrowheads indicate the onset of probe trials for the respective ITIs. Data shown as mean ± SEM. (H) Onset times of the PE signal measured from the end of the previous trial. p = 0.006 by one-way repeated measures ANOVA, *p = 0.028, **p = 0.0067 by Tukey's post hoc test, n = 12 fish.

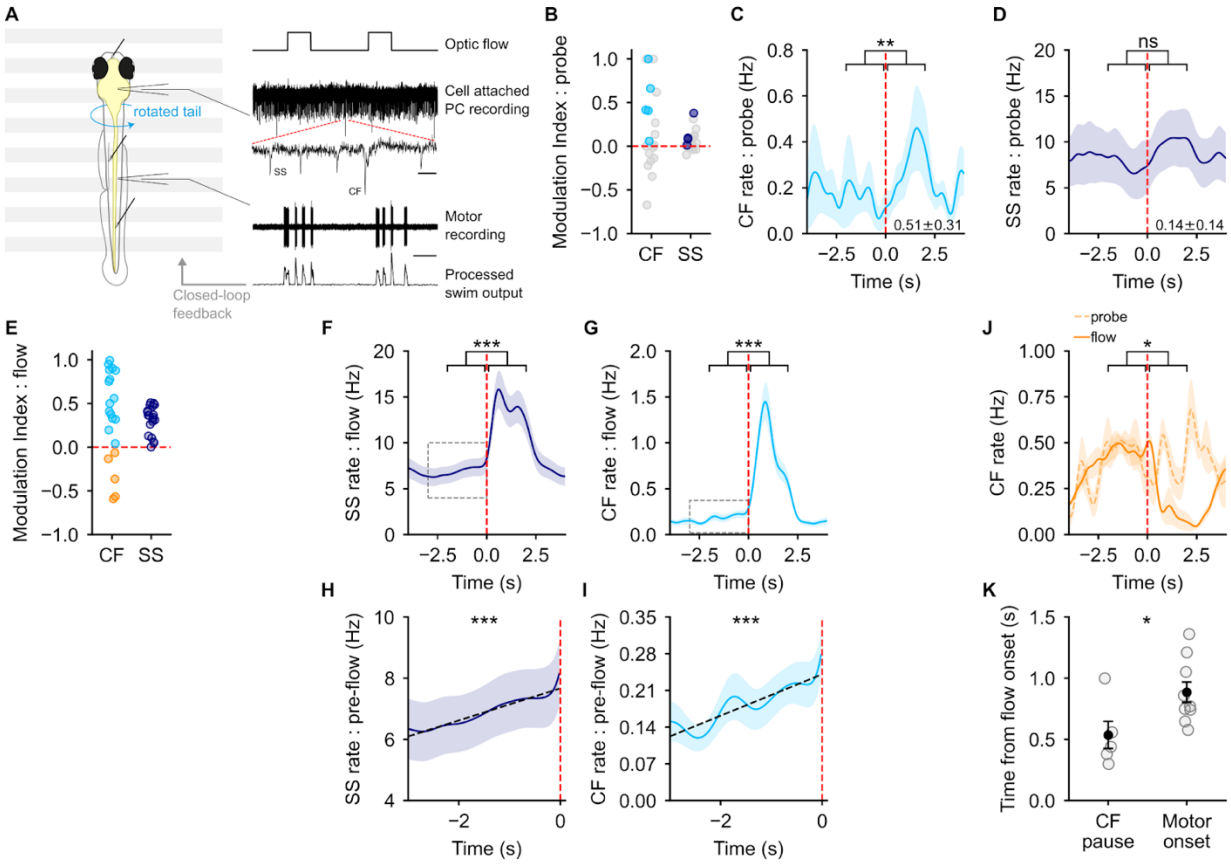

Figure 5. Electrophysiological correlates of prediction and error signals in Purkinje cells
(A) Experimental preparation showing simultaneously recorded Purkinje cell responses and fictive swim output. Scale, zoomed out: 2s ; zoomed in : 20ms. (B) CF and SS modulation indices for probe trials for 20 cells. Cells with significant positive modulation (See Methods) are highlighted. (C) CF rate during probe trials is significantly elevated compared to baseline for the probe responsive cells identified in (B). **p = 0.0097. (D) SS responses of the four probe responsive cells identified in (B). The SS rate did not show a significant increase in probe trials for the SS probe responsive cells identified in (B). ns : p = 0.26. Average modulation indices are inset in (C, D) as mean ± SD. (E) CF input and SS optic flow modulation indices for 20 cells. CF input rate is elevated during optic flow in 15 cells (cyan) and suppressed in 5 cells (orange). SS rate is elevated during optic flow compared to pre-flow levels in all cells (purple). (F) Optic flow triggered SS responses of all cells. ***p = 3.4 x 10^{-5}. (G) Optic flow triggered CF responses of cells with positive modulation indices. ***p = 3.3 x 10^{-5}. (H, I) Pre-trial increase in SS and CF rates in cells with positive modulation indices (zoom of highlighted pre-trial windows in (F, G)). SS: ***p = 3.8 x 10^{-4}, CF : ***p = 1.3 x 10^{-6} by linear mixed-effects. Dashed black lines are linear mixed-effects fits. (J) Optic flow and probe CF responses of cells with negative modulation indices. Pre-probe vs probe : *p = 0.043, probe vs pre-probe p = 0.1. (K) CF suppression does not coincide with motor onset. *p = 0.038, t-test. Traces in (C, F-J) show mean ± SEM. p-values in (C, D, F, G, J) are from paired t-tests. Dashed red lines in (C, D, F-J) indicate the onset of a trial.

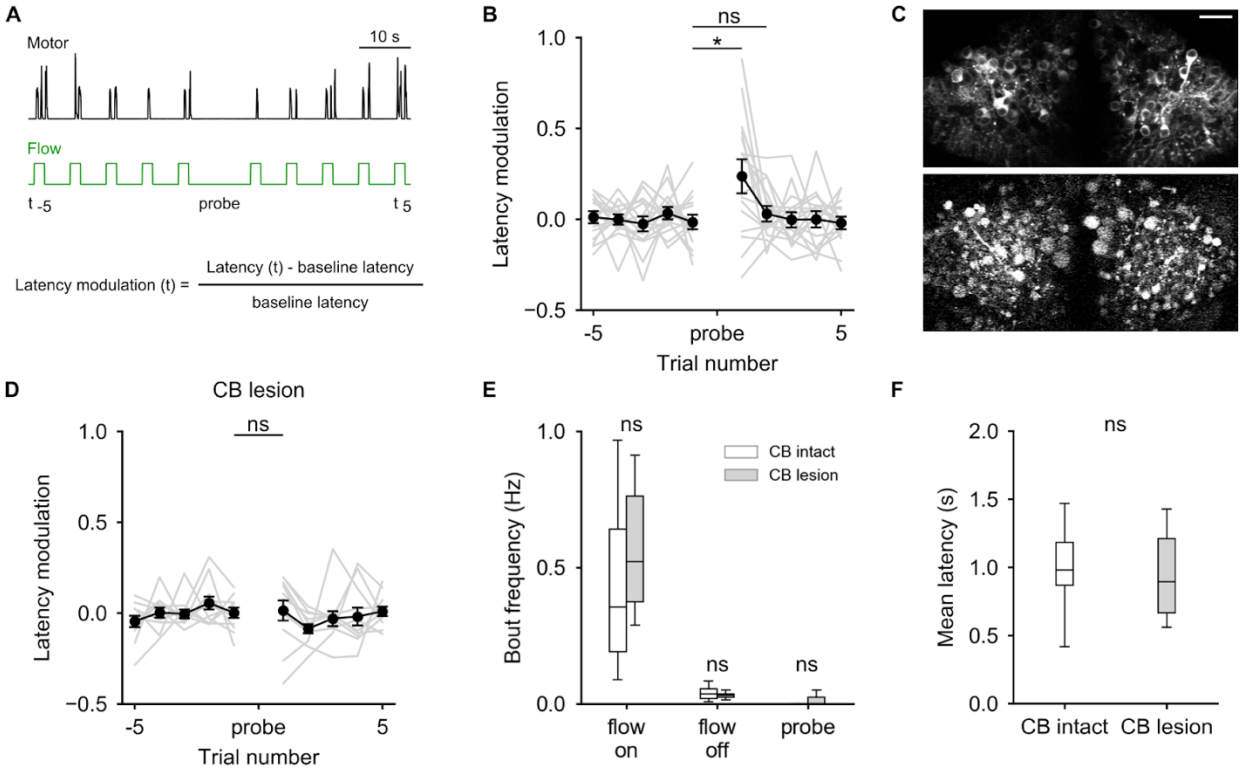

Figure 6. Prediction and error signals in Purkinje cells regulate swim bout latency
(A) Calculating latency modulation for a window of 5 trials before and after a probe trial. Baseline latency is the average latency of the 5 trials before the probe trial. (B) Probe trials cause a transient elevation in latency in the next trial. *p = 0.03 by Wilcoxon signed-rank test, 17 fish. Latency returns to baseline after one trial. ns : p = 0.43. (C) A representative two-photon optical section showing Purkinje cells before lesioning (top) and one hour after lesioning (bottom). (D) Fish tested after lesioning the cerebellum did not show an increase in latency in the trial following a probe trial. p = 0.79 by Wilcoxon signed-rank test, 11 fish. (E, F) Overall behavioral responsiveness remained unaffected by the lesion.

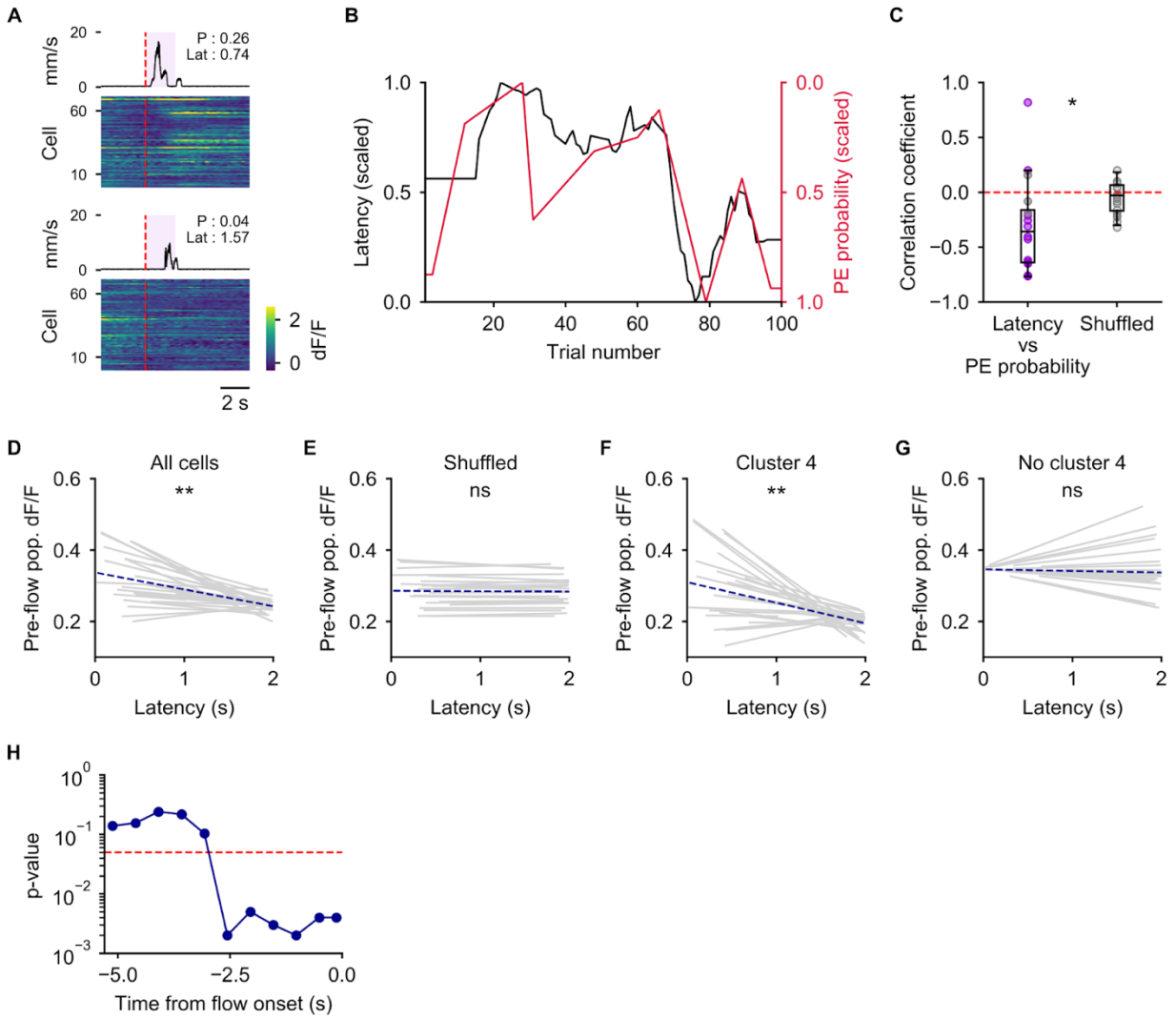

Figure 7. Prediction and error signals in Purkinje cells are correlated with latency at the single trial level

(A) Heatmap showing single trial responses of all cells from a representative fish in two different probe trials with dramatically different trial-wise PE response probabilities. Dashed red line indicates the start of the probe trial. Traces on top of the heatmaps show mean swim velocity for a window of 10 trials around the probe trial. Trial-wise PE response probability and mean latency values are inset. (B) Representative plot showing the negative correlation between latency and interpolated PE response probability. (C) Correlation coefficient between latency and interpolated PE response probability showing a significant negative correlation when compared to trial shuffled correlation. *p = 0.017 by paired t-test, 16 fish. Data points represent individual fish. Purple markers highlight fish with individually significant correlation ($p < 0.05$, from scipy.stats.pearsonr function) compared to chance. Dashed red line is the mean shuffled correlation. (D-G) Linear mixed-effects model fits for individual fish (grey lines, N=27) and the population (dashed blue line) between pre-flow population average dF/F and latency. (D) A significant negative correlation can be seen between pre-flow population activity and latency of all cells. **p = 0.001. (E) No correlation is observed after shuffling the order of trials. p = 0.824. (F, G) Cells in cluster 4 alone account for the correlation observed in (D). **p = 0.004, ns : p = 0.738. (H) p-values of linear mixed-effects model fits for cluster 4 cells for time points ranging from the first frame prior to the onset

of optic flow (same as (F)) to 5s prior to the onset of optic flow. Significant predictive information about latency is present in cluster 4 Purkinje cells up to 2.5s prior to trial onset.

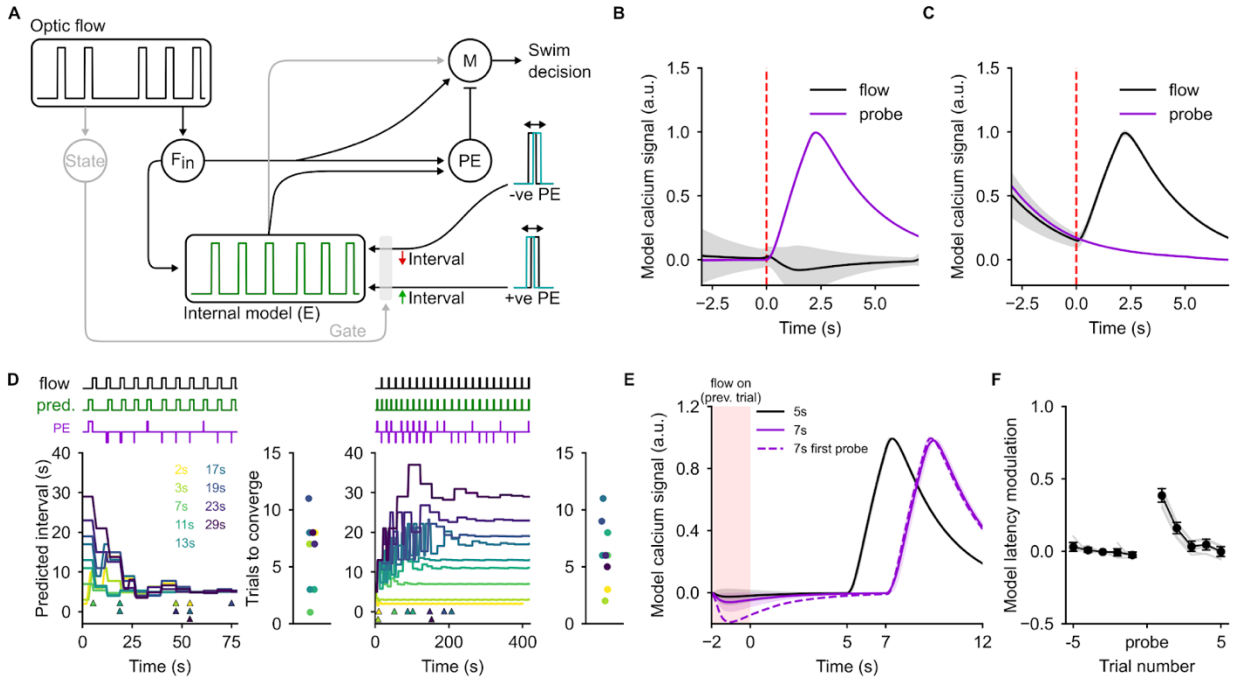

Figure 8. Algorithmic model explains the acquisition of predictive timing representations and their behavioral consequence

(A) Schematic of the algorithmic model. Grey arrows are not part of the simulation and are shown to aid conceptualization. (B, C) Model PE response ((B), cluster 2, 3, 5, 8 like) and flow response ((C), cluster 4 like) are qualitatively similar to experimentally observed responses. Red dashed line indicates the onset of a trial. (D) Left : Predicted time interval in the model converges in experimental timescales to the stimulus interval of 5s from a wide range of values. Right : the model adapts to a wide range of stimulus intervals from an initial timing representation of 5s. Arrows indicate the time at which the model converged to the stimulus interval(s). Initial values in the left panel and stimulus intervals in the right panel are the set of prime numbers (color coded) in the range [2, 29], excluding 5. Trials taken to converge are plotted alongside each panel. Top : representative optic flow (F_{in}), internal model (E) and PE traces from one of the conditions in the corresponding bottom panel with the same time axis. (E) Model PE responses adapt rapidly to a new 7s ITI (purple) within four trials (first probe) from the previously entrained 5s ITI (black). t = 0s represents the end of the previous trial. (F) Modeled latency is transiently elevated after probe trials due to inhibition of locomotor drive by PE. Error bars and shaded regions represent standard deviation.

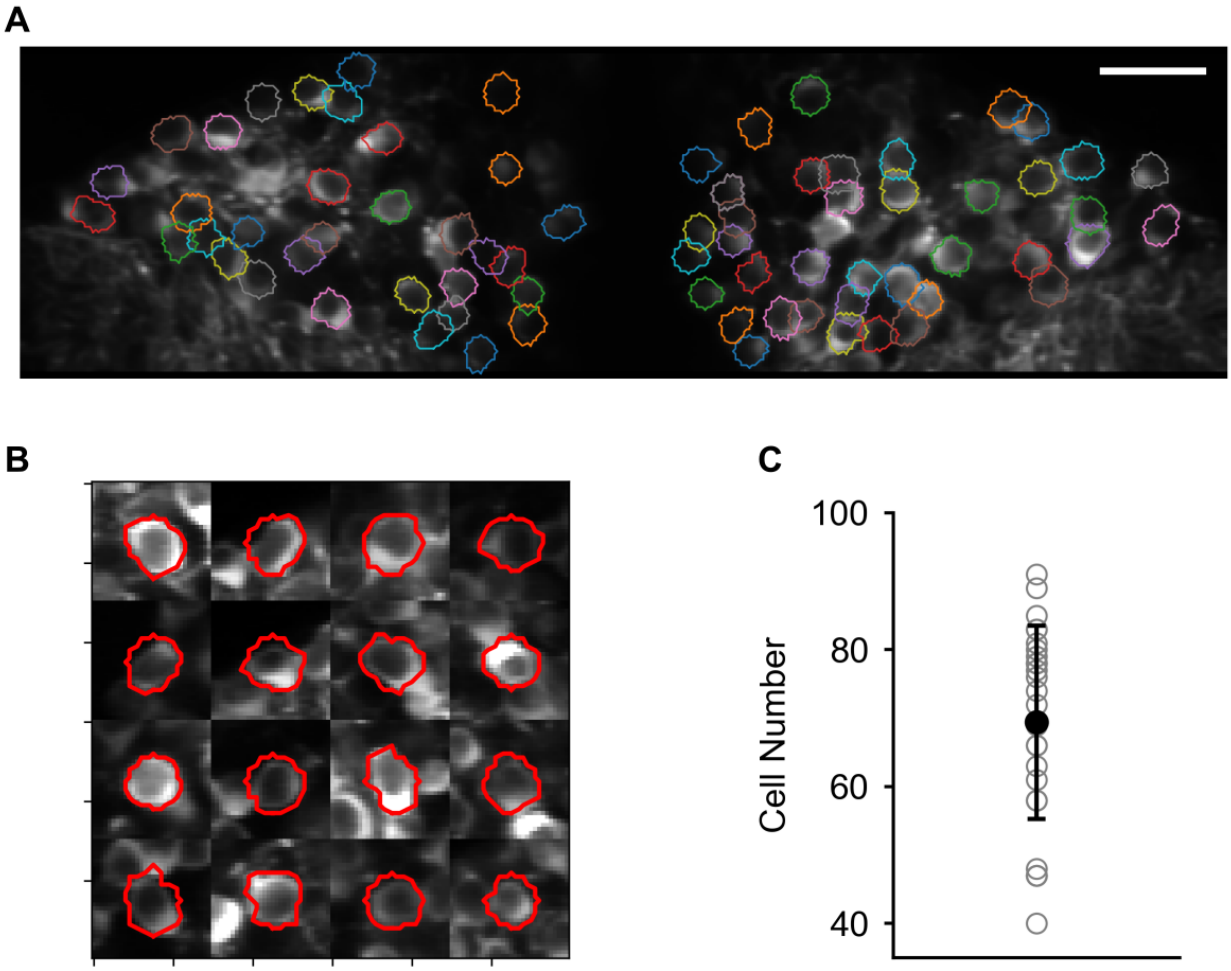

Figure S1. Semi-automated identification of cell boundaries
(A) ROIs consisting of Purkinje cell somata marked using a semi-automated neural network based method. Overlapping pixels in neighbouring ROIs are excluded from dF/F calculation to prevent signal contamination. Scale bar : 20µm. (B) A zoomed-in view of boundaries detected for 16 cells with variable shapes and sizes. (C) The number of cells obtained from 27 fish. We recorded 69 ± 14 cells (mean ± SD) per fish.

Cluster	Mean PE onset (s)	SD (s)	p-value
2	0.28	0.94	$<10^{-5}$
3	0.25	0.49	$<10^{-5}$
5	0.44	0.73	$<10^{-5}$
8	0.40	0.78	$<10^{-5}$

Table S1. Analysis of time-locking of the response seen in probe trials for clusters 2, 3, 5 and 8
The table shows mean and standard deviation of the onset time distributions relative to the onset of probe trials for clusters 2, 3, 5 and 8. The window of analysis spanned ±3 seconds from probe onset. The onset time distributions are centered around the onset of probe trials for all the clusters. P-values estimated by a randomization based test (See Methods) show significant time-locking for all clusters compared to what is expected from a uniform distribution in the ±3 window.

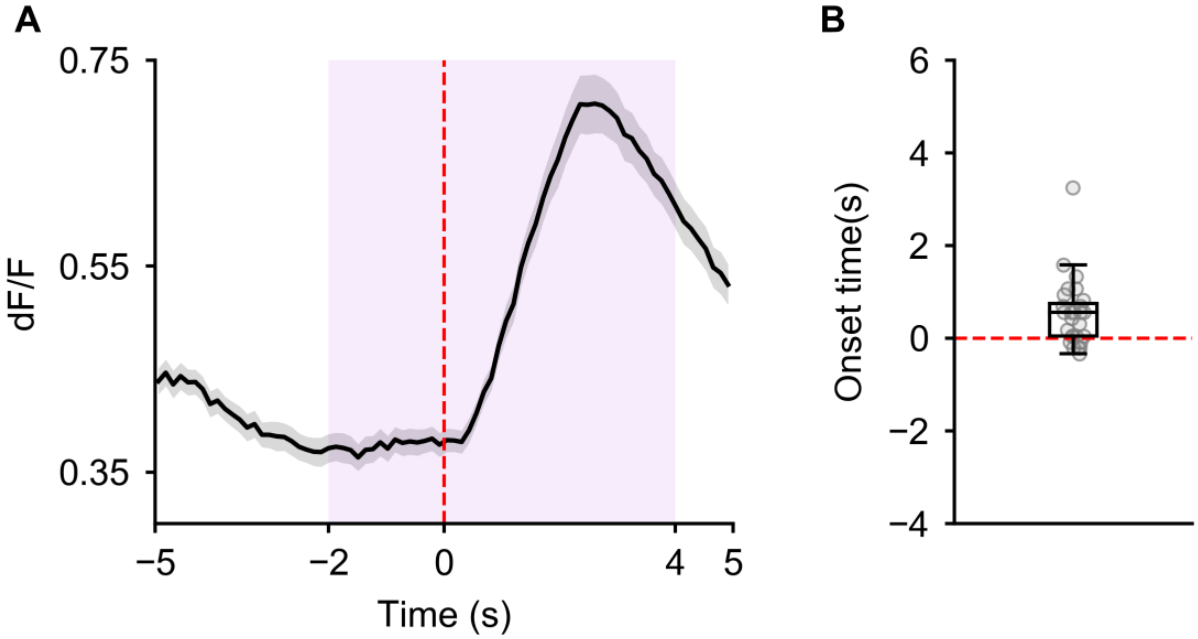

Figure S2. Probe responses are specific to the expected onset time of optic flow.
(A) Average response profile of cells picked for showing a significant increase in activity at any time point within the highlighted window -2s to 4s from the onset of a probe trial. Even with the wide window for detection, responses are sharply tuned to the expected onset time of optic flow (t = 0s). Shaded region represents SEM for 27 fish. (B) Onset times estimated for 27 fish show responses tuned to 0.53 ± 0.73s (mean ± SD). The red dashed line indicates the onset of probe trials.

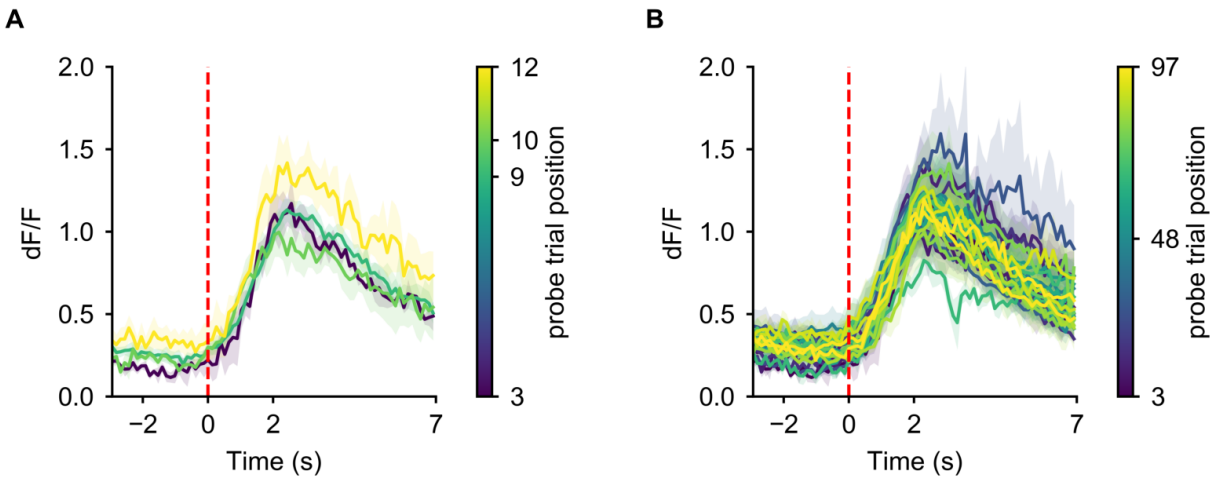

Figure S3. Trial-wise probe triggered average responses of cells which show significant increase in activity in each probe trial

(A, B) Trial-wise average PE signal in the first 4 probe trials (A) and in all probe trials (B). Color scale indicates the position of the probe trial in the experiment. The PE signal in the 3rd trial is indistinguishable from other probe trials later in the experiment. Shaded regions represent SEM across fish.

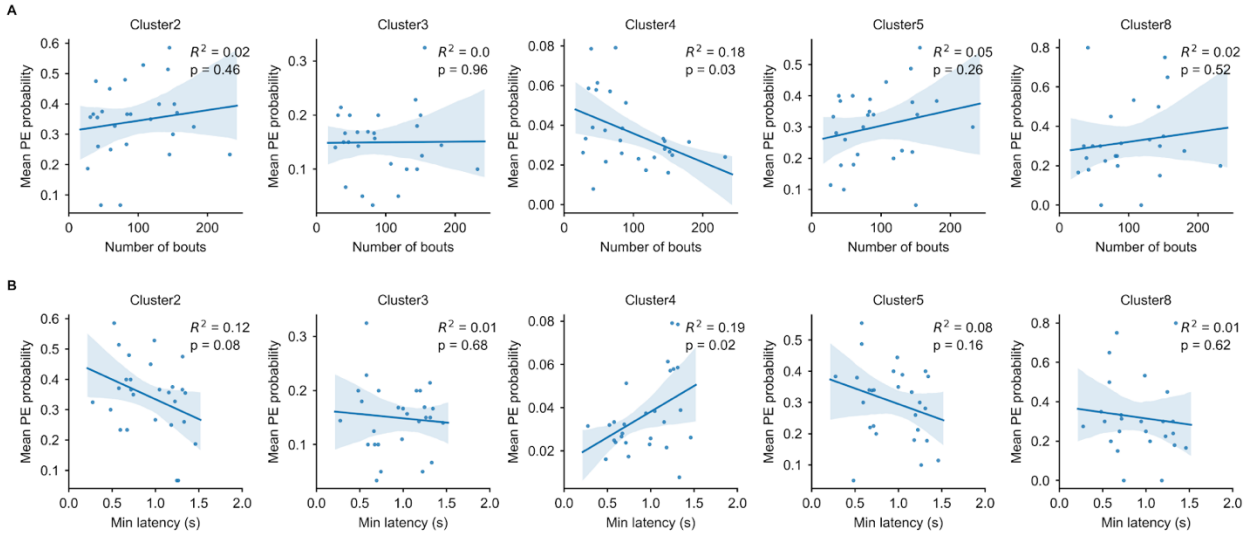

Figure S4. Clusterwise linear regression fits between mean PE response probability and motor variables

(A, B) PE response probability is largely independent of the number of swim bouts (A) or minimum latency (B). Cluster 4 cells show a weak but significant dependence on average population level indicators of behavioral arousal, with lower PE response probability in fish with higher levels of arousal (Cluster 4, A, B). Solid lines show linear regression fits. Shaded regions represent 95% confidence intervals. R^2 for the fits and p-values for Wald test for non-zero slope are inset within each plot. N = 27 fish.

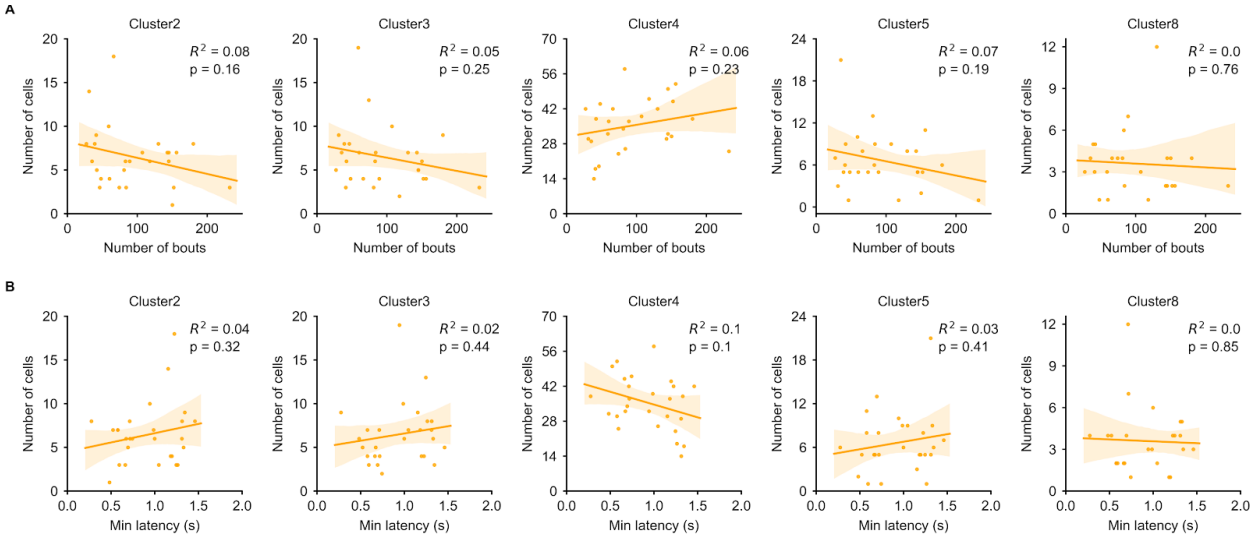

Figure S5. Linear regression fits between clusterwise distribution of cells and motor variables
(A, B) Distribution of cells across the functional clusters is independent of the number of bouts (A) and the minimum latency (B). Solid lines show linear regression fits. Shaded regions represent 95% confidence intervals. R^2 for the fits and p-values for Wald test for non-zero slope are inset within each plot. N = 27 fish.

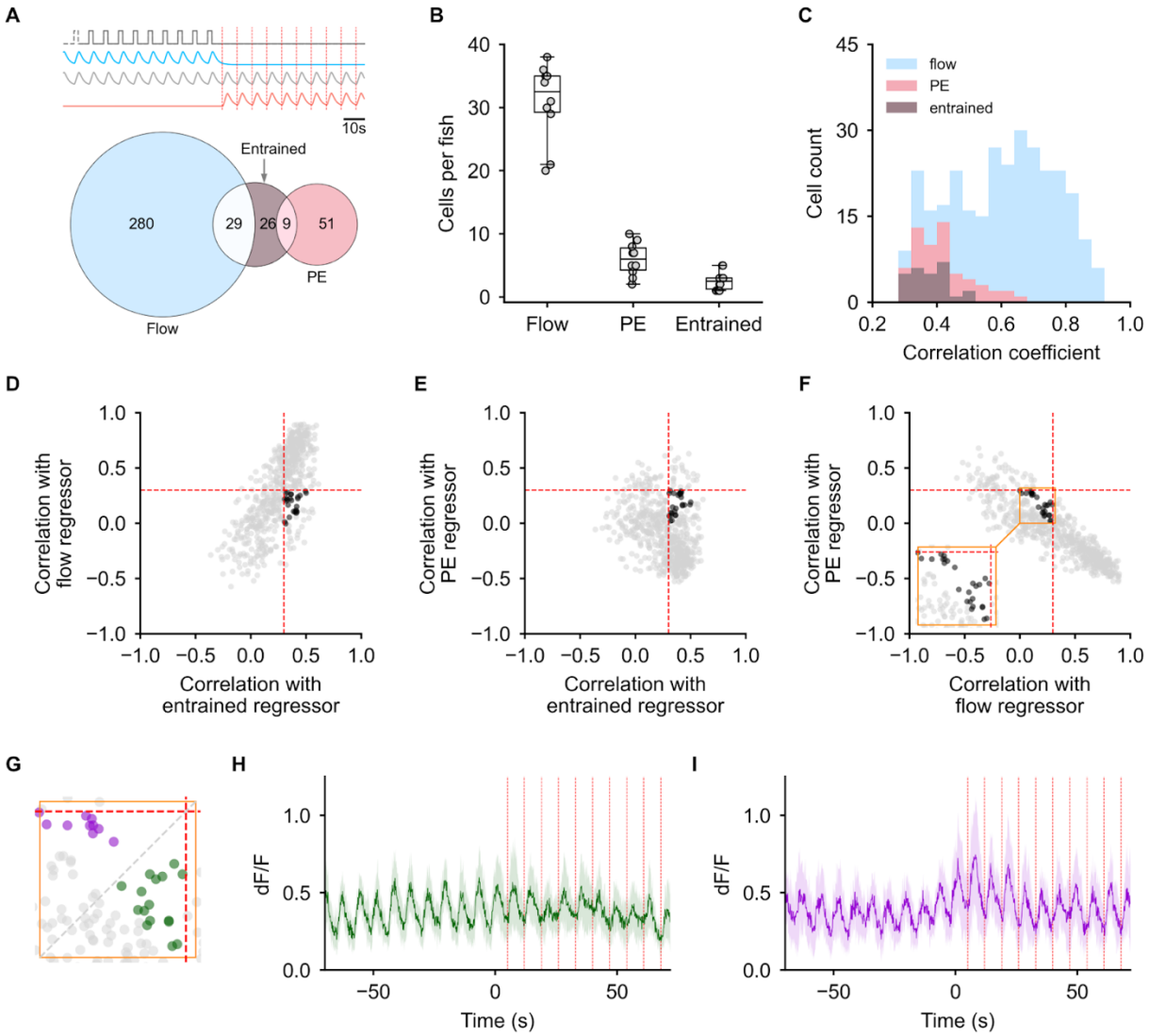

Figure S6. Distribution of cells based on correlation with optic flow, entrained and PE regressors
(A) Top: Optic flow, entrained and PE regressors aligned with the optic flow stimulus. Bottom: distribution of cells showing suprathreshold correlation (threshold = 0.3) with optic flow, PE or entrained regressors. (B) Number of cells per fish classified as optic flow responsive, entrained, or PE. N = 10 fish. (C) Histogram showing the correlation coefficients of cells in each class. (D-F) Correlation coefficients of all cells recorded in this experiment across 10 fish. In all plots, the 26 entrained cells are highlighted in black. (G) A zoomed in window of the region highlighted in (F) with entrained cells that are more optic flow correlated than PE correlated in green and entrained cells that are more PE correlated than optic flow correlated highlighted in purple. Dashed grey diagonal is the line of equality. (H, I) Average response of cells highlighted in green and purple respectively in (G). Shaded regions represent SEM across 8 fish. Dashed red lines in (D-G) indicate the threshold correlation of 0.3. Dashed red lines in (A, H, I) indicate the start time of each consecutive probe trial.

Probe trial	Mean PE onset (s)	SD (s)	p-value
1	0.09	0.33	10^{-4}
2	0.25	0.3	$<10^{-5}$
3	0.39	0.21	$<10^{-5}$
4	0.27	0.44	4×10^{-4}
5	-0.07	0.82	0.08
6	-0.01	0.64	0.01
7	-0.04	0.67	0.02
8	0.14	0.32	$<10^{-5}$
9	0.31	0.32	$<10^{-5}$
10	0.13	0.35	10^{-4}

Table S2. Analysis of onset times of the entrained PE responses across 10 consecutive probe trials
PE responses across 10 consecutive probe trials remain significantly time-locked to the expected onset time of optic flow compared to chance. The onset times and p-values were estimated within a ±2 second window relative to the start of each probe trial. p-values were estimated using a randomization test described in the methods section and indicate whether there is significant time-locking compared to random sampling from a uniform distribution of onset times spanning the ±2 second window.

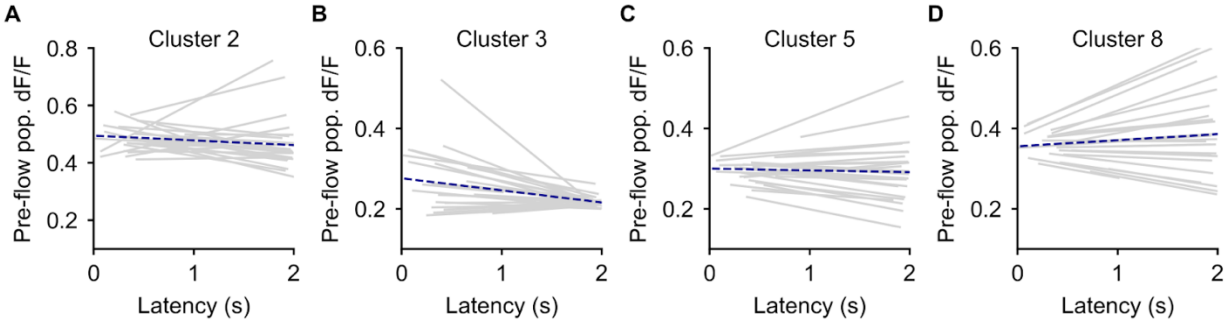

Figure S7. Correlation between pre-trial activity and latency for clusters 2, 3, 5 and 8
(A-D) Linear mixed-effects model fits for clusters 2, 3, 5 and 8 show no significant predictive information about latency in these clusters. N of 27 fish, p-values : A, 0.492; B, 0.069; C, 0.819; D, 0.544.